PHYSICAL REVIEW D **83,** 023518 (2011)

Implications of high-resolution simulations on indirect dark matter searches

Lidia Pieri,[1,*] Julien Lavalle,[2,†] Gianfranco Bertone,[1,‡] and Enzo Branchini[3,§]

[1]*Institut d'Astrophysique de Paris, France, UMR7095-CNRS, Université Pierre et Marie Curie, 98bis Boulevard Arago, 75014 Paris, France*

[2]*Dipartimento di Fisica Teorica, Università di Torino, and INFN, Via Giuria 1, I-10125 Torino, Italy*

[3]*Dipartimento di Fisica, Università di Roma 3, Via della Vasca Navale 84, I-00146 Roma, Italy*

(Received 8 August 2009; revised manuscript received 5 May 2010; published 21 January 2011)

We study the prospects for detecting the annihilation products of dark matter (DM) in the framework of the two highest-resolution numerical simulations currently available, i.e., *Via Lactea II* and *Aquarius*. We propose a strategy to determine the shape and size of the region around the Galactic center that maximizes the probability of observing a DM signal, and we show that, although the predicted flux can differ by a factor of 10 for a given DM candidate in the two simulation setups, the search strategy remains actually unchanged, since it relies on the angular profile of the annihilation flux, not on its normalization. We present mock γ-ray maps that keep into account the diffuse emissions produced by unresolved halos in the Galaxy, and we show that, in an optimistic DM scenario, a few individual clumps can be resolved above the background with the Fermi-LAT. Finally, we calculate the energy-dependent boost factors for positrons and antiprotons and show that they are always of $\mathcal{O}(1)$, and, therefore, they cannot lead to the large enhancements of the antimatter fluxes required to explain the recent PAMELA, ATIC, Fermi, and HESS data. Still, we show that the annihilation of 100 GeV weakly interacting massive particles into charged lepton pairs may contribute significantly to the positron budget.

DOI: 10.1103/PhysRevD.83.023518 PACS numbers: 95.35.+d, 95.30.Cq, 98.35.Gi, 98.70.Sa

I. INTRODUCTION

Despite many observational and theoretical efforts, the nature of dark matter (DM), one of the main components of the Universe, is still unknown.

This has motivated the search for signals arising from the (weak) coupling of the dark sector to ordinary matter and radiation, one of the most promising being self-annihilation. ''Indirect'' DM searches are based on the search for secondary particles (neutrinos, energetic electrons, antimatter, and γ rays) produced by the annihilation or decay of DM particles.

The spectacular increase in the positron ratio above 10 GeV measured by the PAMELA satellite [1], as well as the data collected at the same time on cosmic-ray electrons and positrons by the ATIC [2], HESS [3,4], and Fermi [5] experiments, have given a boost to the phenomenological study of DM models and properties. The PAMELA excess can be interpreted in terms of standard astrophysical sources—see, e.g., Refs. [6–12]—whereas its interpretation as a DM annihilation signal requires unconventional DM particle models—see, e.g., [13,14]—and it is rather severely constrained by the absence of an associated flux of inverse Compton (IC) photons, antiprotons, and γ rays [15–21]. Furthermore, all DM models with a high-annihilation cross section, as needed to reproduce the PAMELA data, would heat and ionize the baryons in the early Universe; the constraints that can be set on these models from cosmic microwave background (CMB) data do not rely on uncertain assumptions of the DM distribution in virialized structures and can, therefore, be regarded as robust and model-independent [22–24].

In this paper, we discuss a self-consistent study of the antimatter flux arising from DM annihilations, along with the associated γ-ray flux. A comprehensive outlook of the observable effect of a given DM candidate can, indeed, be useful in the case of a future claim for a DM signal.

Both messengers can, indeed, be produced from the hadronization (decay) of the DM annihilation final states if they are quarks (heavy bosons). In addition, the electrons or positrons injected from DM annihilation produce γ rays from inverse Compton scattering (ICS) with the interstellar radiation fields; although negligible in the case of hadronizing annihilation final states with respect to the π^0 decay yield, this γ-ray production could be sizable for leptophilic DM models. In fact, a γ-ray signal from DM annihilation would provide the ''cleanest'' evidence for DM, since photons do not suffer deflection and energy losses in the local Universe. Besides peculiar spectral features such as annihilation lines and final-state radiation [25–29], an interesting smoking gun for DM would be the detection of many γ-ray sources with identical spectra and no counterpart at other wavelengths [30–42]. In addition, a characteristic DM signature may also be found in the angular power spectrum of the diffuse γ-ray background [43–51].

We consider here four benchmark models, representative of the most commonly discussed DM candidates and of the models that have been invoked to explain the cosmic lepton data discussed above.

*lidia.pieri@gmail.com
†lavalle@to.infn.it
‡gf.bertone@gmail.com
§branchin@fis.uniroma3.it

The issue of the spatial distribution of DM can be tackled in different ways. Analytic methods based on the excursion set theory [52] provide a useful, although approximate, insight on the evolution of DM halos [53]. N-body simulations are the best way to study the highly nonlinear processes involved in the evolution of substructures. Unfortunately, they can only probe a limited range of halo masses and scales. The latest numerical simulations of Milky Way (MW) -sized DM halos [54–57] are able to resolve $\sim 100,000$ substructures down to $\sim 10^{4.5} M_\odot$ at the present epoch. The evolution of micro-halos with size close to the free streaming mass can only be studied by simulating a small region at very high redshifts [58].

As a consequence, modeling the properties of the Galactic subhalos requires aggressive extrapolations, which are usually performed by means of analytic, Monte Carlo, or hybrid techniques and, therefore, are potentially affected by large theoretical uncertainties. In this work, we rely on the results of the *Aquarius* [56,57] and *Via Lactea II* [55] numerical simulations. For γ rays, we then apply the hybrid method of [40] to compute the expected annihilation flux of γ-ray photons produced within our Galaxy. For antimatter, we use the method developed in [59] to obtain the boost factor to cosmic-ray fluxes due to the presence of the same population of subhalos. In the photon flux prediction, we also need to account for the extragalactic contribution and the diffuse Galactic foreground. In order to model such contributions, we have scaled down the signal measured by EGRET at $E > 3$ GeV by 50%. This reduction accounts for the fact that the Fermi data do not confirm the so-called Galactic excess measured by EGRET either in the strips $10^\circ < |b| < 20^\circ$ [60] or at larger latitudes, as we have verified by comparing the Fermi maps made available by [61] with the EGRET data [62]. The antimatter flux is obtained by solving the transport equation for high-energy positrons and antiprotons produced by DM annihilation and ignoring contributions from astrophysical sources. In this case, the background produced by spallation processes is taken from [63,64].

The main aim of this work is to assess the reliability of this approach, i.e., that modeling the expected DM annihilation flux by extrapolating the results of state-of-the-art numerical simulation provides robust predictions that can be used to assess the possibility of detecting the annihilation signals of both photons and antimatter with current detectors.

The paper is organized as follows: In Sec. II, we describe our models for DM halos and their substructures, which contribute to the cosmological part of the DM annihilation signal. In Sec. III, we introduce our particle physics benchmark models that determine the amplitude, shape, and features of the annihilation spectrum. Our model predictions for the γ-ray and antimatter fluxes are described in Secs. IV and V, respectively. Section VI shows the inverse Compton scattering computation for the particle physics benchmarks for which it is relevant. Finally, we discuss our results and conclude in Sec. VII.

In this work, we adopt the WMAP 5-yr [65] flat ΛCDM model ($\Omega_m = 0.26$, $\Omega_\Lambda = 0.74$, $\sigma_8 = 0.79$, $n_s = 0.96$, and $H_0 = 72\ \mathrm{km\,s^{-1}\,Mpc^{-1}}$).

II. MODELING DM HALOS AND SUBHALOS

The N-body experiments *Aquarius* [56,57] and *Via Lactea II* [55] have simulated the DM halo of a MW-like galaxy in a flat ΛCDM model with cosmological parameters consistent, within the errors, with those that best fit the WMAP 1-yr and WMAP 3-yr data, respectively (*Aquarius* used $\Omega_m = 0.25$, $\Omega_\Lambda = 0.75$, $\sigma_8 = 0.9$, $n_s = 1$, and $H_0 = 73$ km/s/Mpc; while *Via Lactea II* used $\Omega_m = 0.24$, $\Omega_\Lambda = 0.76$, $\sigma_8 = 0.88$, $n_s = 0.97$, and $H_0 = 74$ km/s/Mpc). Thanks to the unprecedented high resolution, these simulations were able to resolve substructures down to masses as small as $\sim 10^{4.5} M_\odot$ (*Aquarius*) and $\sim 10^5 M_\odot$ (*Via Lactea II*) to characterize their inner structure, to trace their spatial distribution within the main halo, and to model the dependence of their shape parameter (the concentration) on the distance from the Galactic center (GC). For the *Via Lactea II*, we will consider subhalos selected by mass as in [66], rather than by peak circular velocity as in [55]. We have checked that using either subhalo parametrization does not significantly affect our predictions for the detectability of the annihilation signal.

Following the results of numerical simulations, the DM distribution in the MW halo consists of two separate phases: a smoothly distributed component (main halo) and a clumpy component made of virialized substructures (subhalos). We, therefore, ignore the presence of caustics, streams, and all other possible inhomogeneities that do not correspond to virialized structures.

Following Ref. [66], we model the total density profile of the MW DM halo (smooth halo and subhalos) by a Navarro, Frenk, and White (NFW) profile in the case of *Via Lactea II*:

$$\rho_{\mathrm{tot}}^{VLII}(R) = \frac{\rho_s}{\frac{R}{r_s}\left(1 + \frac{R}{r_s}\right)^2}, \tag{1}$$

where R is the distance from the GC. We note that the authors of Ref. [56] found a steeper profile close to the GC for *Via Lactea II*, scaling like $R^{-1.2}$ instead of R^{-1}. Given the uncertainty in the determination of the slope close to the GC due to resolution effects, we conservatively choose here to stick to the NFW case.

For the *Aquarius* configuration, we use a shallower Einasto profile with $\alpha = 0.17$ [55,57]:

$$\rho_{\mathrm{tot}}^{Aq}(R) = \rho_s \exp\left\{-\frac{2}{\alpha}\left[\left(\frac{R}{r_s}\right)^\alpha - 1\right]\right\}. \tag{2}$$

The best-fitting values of the scale density, ρ_s, and the scale radius, r_s, are listed in Table I. The aforementioned density profiles are displayed in Fig. 1 with solid lines.

TABLE I. Characteristic values for the smooth and clumpy components of the DM distribution modeled after the *Via Lactea II* and *Aquarius* results. $R_{\rm vir}$ = virial radius, i.e., the radius within which the numerical simulations define the halo. M_h = MW mass. r_s = scale radius of the overall DM distribution. ρ_s = scale density of the overall DM distribution. $\mathcal{F}_0$ = normalization to unity for the normalized subhalo mass function. ρ_a = normalization of the subhalo mass-density profile for the *Aquarius* configuration. R_a = scale radius of the subhalo distribution. $\langle\rho_\odot\rangle$ = averaged local DM density (at 8 kpc from the GC). $N_{\rm sub}$ = total number of subhalos. $M^{\rm tot}_{\rm sub}$ = total mass in subhalos. $f^{\rm tot}_{\rm sub}$ = clumpiness fraction, defined as $M^{\rm tot}_{\rm sub}/M_h$. Subhalo abundances are computed assuming the Roche criterion.

	Via Lactea II	*Aquarius*
$R_{\rm vir}$[kpc]	402	433
$M_h[M_\odot]$	1.93×10^{12}	2.5×10^{12}
r_s[kpc]	21	20
$\rho_s[10^6 M_\odot{\rm kpc}^{-3}]$	8.1	2.8
$\mathcal{F}_0[M_\odot^{-1}]$	10^{-6}	3.6×10^{-6}
$\rho_a[M_\odot{\rm kpc}^{-3}]$	...	2840.3
R_a[kpc]	85.5	199
$\langle\rho_\odot\rangle$[GeV/cm^3]	0.42	0.57
$N_{\rm sub}$	2.8×10^{16}	1.1×10^{15}
$M^{\rm tot}_{\rm sub}(<R_{\rm vir})[M_\odot]$	1.05×10^{12}	4.2×10^{11}
$f^{\rm tot}_{\rm sub}(<R_{\rm vir})$	0.53	0.17

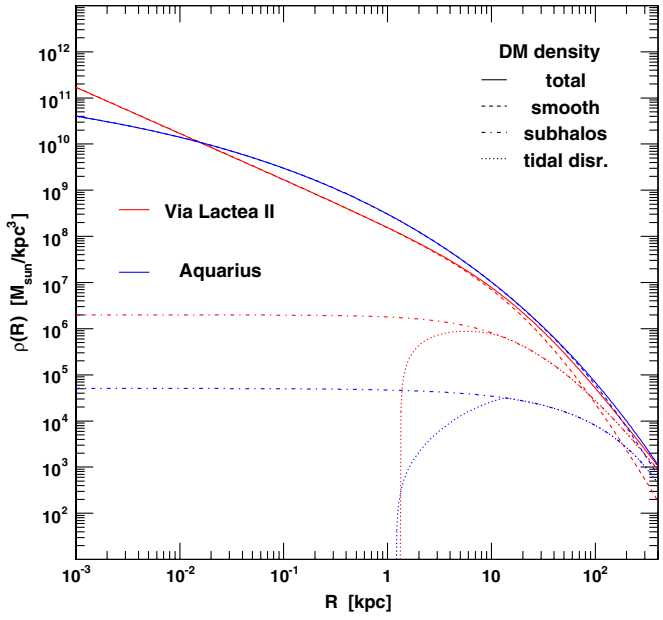

FIG. 1 (color online). Mass-density profiles of the MW halo components for the *Via Lactea II* and *Aquarius* cases. For each setup, the solid line represents the sum of all components, while the dashed line is the smooth halo component, and the dotted-dashed line accounts for the subhalo component. The dotted line exhibits the subhalo component when the tidal disruption, according to the Roche criterion, is implemented.

M_h and $M_{\rm sub}$ being the main halo and subhalo masses, the joint spatial and mass subhalo distribution is given by

$$\frac{d\rho_{\rm sh}(M_{\rm sub},R)}{dM_{\rm sub}} = \rho_{\rm sub}(R)\mathcal{F}(\mu,M_{\rm sub}). \tag{3}$$

The previous equation provides the mass density in the form of subhalos per unit subhalo mass. The normalized mass function $\mathcal{F}(\mu,M_{\rm sub})$, which carries units of inverse mass, is defined a bit further in Eq. (6).

In the case of *Via Lactea II*, the global subhalo mass-density profile $\rho_{\rm sub}(R)$ is best fitted by the so-called anti-biased relation [55,66]:

$$\rho^{VLII}_{\rm sub}(R) = \frac{\rho^{VLII}_{\rm tot}(R)(R/R_a)}{(1+\frac{R}{R_a})}. \tag{4}$$

Given the NFW overall profile $\rho^{VLII}_{\rm tot}(R)$, we see that the subhalo distribution is cored below a scale radius R_a, while it asymptotically tracks the smooth profile beyond. The procedure to obtain this antibiased profile is detailed in the Appendix, where it is shown that R_a is actually fixed by the mass fraction in the form of subhalos.

It is worth noticing that the antibiased spatial distribution is specific to the choice of using a subhalo selection based on the subhalo mass. Subhalos selected by $V_{\rm max}$ or before accretion would lead to less antibias [67], suggesting that this spatial feature is mainly due to tidal stripping.

For *Aquarius*, an Einasto shape is also found for the spatial distribution of subhalos [56,57], which leads to the following global subhalo mass-density profile:

$$\rho^{Aq}_{\rm sub}(R) = \rho_a \exp\left\{-\frac{2}{\alpha}\left[\left(\frac{R}{R_a}\right)^\alpha - 1\right]\right\}, \tag{5}$$

with $\alpha = 0.678$, and where $\rho_a \equiv k_V M^{\rm tot}_{\rm sub} = k_V f^{\rm tot}_{\rm sub} M_{\rm MW}$ is fixed from the total subhalo mass (or the mass fraction, equivalently) and the parameter k_V, which normalizes the exponential term to unity within the Galactic volume.

The normalized subhalo mass function used in both subhalo distributions reads

$$\mathcal{F}(\mu,M_{\rm sub}) \equiv \mathcal{F}_0\left[\frac{M_{\rm sub}}{M_\odot}\right]^{-\mu}, \tag{6}$$

where $\mathcal{F}_0$, which carries units of inverse mass, allows the normalization of the mass integral of $\mathcal{F}$ to unity in the surveyed mass range. Following [66], we use the fiducial value of $\mu = 2$ in the *Via Lactea II* configuration and test the dependence on the mass slope, introducing $\mu = 1.9$ in the *Aquarius* configuration [55,57]. We emphasize that this small difference in μ will induce quite strong differences in the total subhalo number and mass fraction, while minor differences are observed from the simulations themselves. Indeed, we extrapolate the mass function down to a subhalo mass of $10^{-6}M_\odot$, i.e., ~10 orders of magnitude below the actual simulations' resolution, which explains how such large differences can arise.

Note that to get the subhalo number density from the mass density, one can use the trivial following relation:

$$\frac{dN_{\rm sh}(M_{\rm sub}, R)}{dM_{\rm sub}dV} = \frac{1}{\langle M_{\rm sub}\rangle}\frac{d\rho_{\rm sh}(M_{\rm sub}, R)}{dM_{\rm sub}}, \tag{7}$$

where $\langle M_{\rm sub}\rangle \equiv \int dmm\mathcal{F}(\mu, m) = M^{\rm tot}_{\rm sub}/N_{\rm sub}$ is the average subhalo mass. This relation is valid for any configuration.

In the following, we will consider that $M_{\rm min} = 10^{-6}M_\odot$ and $M_{\rm max} = 10^{-2}M_h$. The logarithmic mass slope μ is steeper in the *Via Lactea II* configuration than in the *Aquarius* configuration, which strongly increases the relative weight of the lightest subhalos to the total mass (and therefore to the total annihilation rate) in the former case. All the parameters used for the above subhalo distributions are listed in Table I. They are set to match the results of the corresponding N-body simulations in the resolved subhalo mass ranges. In the case of *Via Lactea II*, we impose that 10% of the MW mass, M_h, consists of virialized structures with masses in the range $[10^{-5}M_h, 10^{-2}M_h]$. In the case of *Aquarius*, we require that 13.2% of M_h is concentrated in subhalos with masses in the range $[1.8\times10^{-8}M_h, 10^{-2}M_h]$. The total mass fraction in the form of subhalos $f^{\rm tot}_{\rm sub}$ is then such that

$$f^{\rm tot}_{\rm sub}M_h = M^{\rm tot}_{\rm sub} \equiv 4\pi\int_0^{R_{\rm vir}} drr^2\int_{M_{\rm min}}^{M_{\rm max}} dm\frac{d\rho_{\rm sh}(m, r)}{dm}. \tag{8}$$

Finally, we can now define the smooth dark matter component for both configurations from the difference between the total and subhalo components:

$$\rho_{\rm sm}(R) = \rho_{\rm tot}(R) - \rho_{\rm sh}(R). \tag{9}$$

We note that the MW mass in both simulations agrees, within the errors, with the recent observational estimates of [68] based on the so-called timing argument [69].

A word of caution is required for the subhalo distribution near the GC (e.g., [70]). Since the subhalo number density at galactocentric distances of 8 kpc or less is poorly constrained by numerical simulations, we calculate this function by extrapolating the behavior at larger distances. Tidal effects may disrupt subhalos in the central regions of the Galaxy, which severely depletes the subhalo population. To account for this effect, we adopt the Roche criterion [71]: a subhalo is destroyed when its scale radius r_s is larger than the tidal radius, i.e., the radius at which the tidal forces of the host potential equal the self-gravity of the subhalo

$$r_{\rm tid}(R) = \left(\frac{M_{\rm sub}}{3M_h}\right)^{1/3}R. \tag{10}$$

Clearly, the amplitude of the effect depends on the subhalo mass and its distance from the GC. In Fig. 2, we plot the largest mass $M^{\rm max}_{\rm sub}$ of a subhalo that survives tidal disruption as a function of R—the effect on the overall subhalo mass-density profile is illustrated by the dotted curves in Fig. 1. Subhalos are shown to be almost completely disrupted within $R \sim 2$ kpc. As shown by [31], the effect on the total γ-ray flux is negligible, since the main contribution at small distances from the GC is given by the smooth halo, while the subhalo contribution is subdominant. This turns out to be the case also for the antimatter flux, as we will show, and as already pointed out by [72]. We will discuss this point in greater detail in Sec. V C 1.

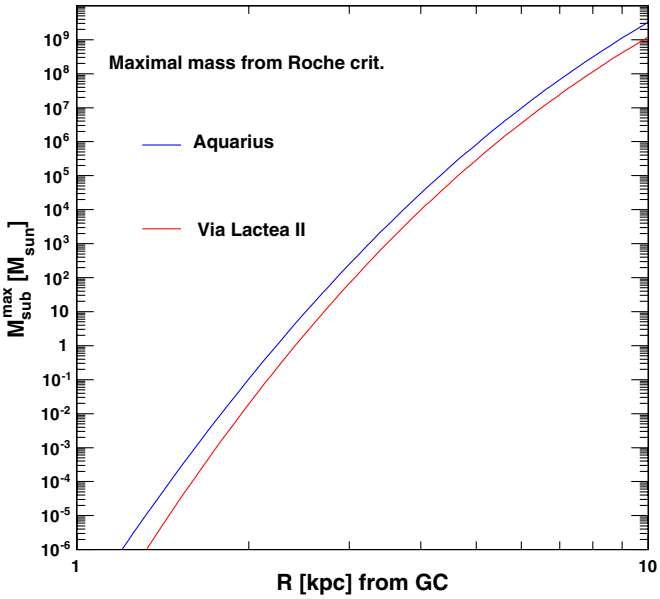

FIG. 2 (color online). Maximum subhalo mass that can be found at distance R from the GC, according to the Roche criterion used in this paper.

A very informative quantity that describes the inner shapes of subhalos is their concentration parameter, defined as the ratio between r_{200} (the radius that encloses an average density equal to 200 times the critical density of the Universe) and the scale radius $c_{200} \equiv r_{200}/r_s$. In general, this quantity is not constant but depends on the subhalo mass and on the distance from the GC. Following the numerical results of [55–57,66], we can parametrize these dependences as follows:

$$c_{200}(M_{\rm sub}, R) = \left(\frac{R}{R_{\rm vir}}\right)^{-\alpha_R}\left\{C_1\left[\frac{M_{\rm sub}}{M_\odot}\right]^{-\alpha_1} + C_2\left[\frac{M_{\rm sub}}{M_\odot}\right]^{-\alpha_2}\right\}. \tag{11}$$

The best-fitting parameters for the *Via Lactea II* and *Aquarius* simulations are listed in Table II. In Fig. 3, we have plotted the mass dependence of the concentration parameter at the virial radius ($R = R_{\rm vir}$) that can be thought of as the concentration parameters of subhalos located at the edge of the simulated MW-like halo, i.e., of field halos. We have also plotted the concentration parameters computed at the Sun position ($R = 8$ kpc), which provides additional information on the potential antimatter yield by featuring the local subhalo properties. From the plot,

TABLE II. Parameters used for the fit to the concentration parameter of subhalos.

	Via Lactea II	*Aquarius*
α_R	0.286	0.237
C_1	119.75	232.15
C_2	−85.16	−181.74
α_1	0.012	0.0146
α_2	0.0026	0.008

we notice that subhalos in the *Aquarius* experiment are more concentrated than in *Via Lactea II* at all masses, a discrepancy that reflects the larger power spectrum normalization (σ_8) assumed in the *Aquarius* experiment.

III. PARTICLE PHYSICS BENCHMARKS

In order to study the dependence of the results on particle physics parameters, we show the results relative to four different benchmark models.

Benchmark A is representative of a class of models in the supersymmetric (SUSY) parameter space that annihilate predominantly to $b\bar{b}$. In order to maximize the annihilation flux, we chose a light neutralino mass $m_\chi = 40$ GeV.

Benchmark B is also representative of a class of SUSY models. The DM particle mass is, in this case, $m_\chi = 100$ GeV, thus allowing annihilation to W^+W^-, which is assumed to constitute the dominant annihilation channel.

Benchmark C provides a "minimal" solution to the rising positron ratio measured by PAMELA, without attempting to address higher-energy (ATIC and Fermi) data.

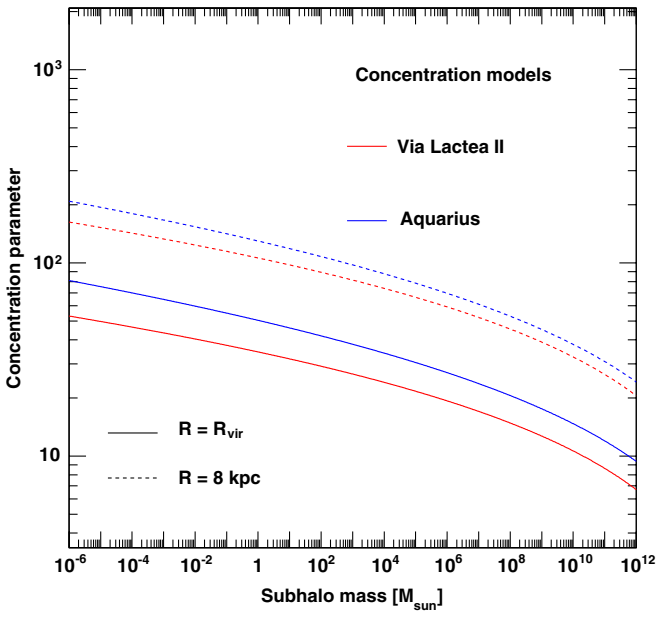

FIG. 3 (color online). Concentration parameter as a function of the halo mass as found in *Via Lactea II* and *Aquarius*, computed at the virial radius $R_{\rm vir}$ and at the Earth–GC distance $R = 8$ kpc.

TABLE III. Benchmark particle physics models. The annihilation cross section is $\langle\sigma v\rangle = 3 \times 10^{-26}$ cm^3 s^{-1}.

Model	m_χ [GeV]	Final state
A	40	$b\bar{b}$
B	100	W^+W^-
C	100	e^+e^-
D	2000	$\tau^+\tau^-$

The mass is, in this case, $m_\chi = 100$ GeV, thus barely above the PAMELA energy range and the leading annihilation channel e^+e^-.

Benchmark D, finally, represents a class of candidates that attempt to explain the cosmic lepton data up to TeV energies. We have adopted, as, e.g., in Ref. [73], $m_\chi = 2000$ GeV and annihilation to $\tau^+\tau^-$.

We have used, in all cases, a thermal annihilation cross section $\langle\sigma v\rangle = 3 \times 10^{-26}$ cm^3 s^{-1}. The parameters of the four benchmark models are summarized in Table III.

IV. GAMMA RAYS

The expected γ-ray flux from DM annihilation, Φ_γ, can be factorized in two terms that depend on the properties of the DM particle, Φ_{PP}, and on their spatial distribution along the line of sight, $\Phi_{\rm los}$:

$$\Phi_\gamma(m_\chi, E_\gamma, M, r, \Delta\Omega) = \Phi_{PP}(m_\chi, E_\gamma) \times \Phi_{\rm los}(M, r, \Delta\Omega) \tag{12}$$

in units of inverse area and inverse time. Here, m_χ is the DM particle mass, M the DM halo mass, r the position inside the halo, and $\Delta\Omega$ the angular resolution of the instrument (in the case of Fermi, for energies above $\sim$1 GeV, one has $\Delta\Omega \sim 10^{-5}$ sr).

The term Φ_{PP} describes the number of photons yielded in a single annihilation, and can be written as

$$\Phi_{PP}(M, E_\gamma) = \frac{1}{4\pi} \frac{\langle\sigma v\rangle}{2m_\chi^2} \int_{E_\gamma}^{m_\chi} \sum_f \frac{dN_\gamma^f}{dE_\gamma} B_f dE_\gamma. \tag{13}$$

Here, f is the final state, B_f is the branching ratio, and $\langle\sigma v\rangle$ denotes the thermal annihilation cross section that reproduces the observed cosmological abundance. dN_γ^f/dE_γ is the differential annihilation photon spectrum that we take from [74].

The term $\Phi_{\rm los}$ represents the number of annihilation events along the line of sight. It is obtained by integrating the square of the DM mass density

$$\Phi_{\rm los}(M, r, \Delta\Omega) = \iint_{\Delta\Omega} d\theta d\phi \int_{\rm los} d\lambda \times \left[\frac{\rho_{\rm DM}^2(M, c, r(\lambda, \theta, \phi))}{\lambda^2} J(x, y, z|\lambda, \theta, \phi)\right]. \tag{14}$$

Here, J is the Jacobian determinant, and c the concentration parameter. In the case of the smooth halo of the MW, $M = M_h$, and c is fixed by the output of N-body simulations, while for the subhalos, $M = M_{\rm sub}$, and c is a function of mass and position: $c = c_{200}(M_{\rm sub}, R)$, as defined in Eq. (11). The integration has been performed over a solid angle of 10^{-5} sr.

The γ-ray annihilation flux receives contributions from three different sources that we model separately:

(i) the DM smoothly distributed in the MW halo,
(ii) the DM within Galactic subhalos,
(iii) and the DM in extragalactic halos and their substructures.

To compute the first contribution, we simply consider the mass-density profile in Eq. (1) or Eq. (2) in the integral of Eq. (14).

To compute the second contribution, one would need to consider all $\sim 10^{16}$ substructures down to the cutoff mass of $10^{-6} M_\odot$, which is unfeasible. One possibility would be to integrate the subhalo distribution [Eq. (4) or Eq. (5)]. This represents the mean annihilation flux, while one of the scopes of this work is to assess the possibility of detecting isolated DM subhalos. To circumvent the problem, we follow the hybrid approach of [40], i.e., we first compute the mean flux, and then we use Monte Carlo techniques to account for the closest and brightest subhalos that one may hope to detect as isolated sources.

More specifically, the mean flux along the line of sight is obtained by integrating the following expression:

$$\Phi_{\rm los}^{\rm sub}(M_h, R, \Delta\Omega) \propto \int_{M_{\rm sub}} dM_{\rm sub} \int_c dc \iint_{\Delta\Omega} d\theta d\phi \times \int_\lambda d\lambda [\rho_{sh}(M_h, M_{\rm sub}, R) P(c) \times \Phi_{\rm los} J(x, y, z|\lambda, \theta, \phi)]. \quad (15)$$

Here, $\Phi_{\rm los}$ represents the contribution from each subhalo, computed by integrating Eq. (14) in the range $[d - r_{\rm tid}, d + r_{\rm tid}]$, with d as the distance to the object. This quantity is then convolved with the subhalo distribution [Eq. (4) or Eq. (5)].

$P(c)$ represents the probability distribution function of the concentration parameter. Following [75], we model it as a log-normal distribution with dispersion $\sigma_c = 0.14$ and mean value $\bar{c}$:

$$P(\bar{c}, c) = \frac{1}{\sqrt{2\pi}\sigma_c c} e^{(-\{[\ln(c) - \ln(\bar{c})]/\sqrt{2}\sigma_c\}^2)}. \quad (16)$$

To model the fluctuations over the mean flux, we compute the annihilation flux from the nearest and brightest subhalos in 10 independent Monte Carlo realizations. For this purpose, we consider only those subhalos whose distance from the Sun is less than the maximum between: (i) the radius of the sphere centered on the Sun, within which lie about 500 halos; and (ii) the distance at which the photon flux from a subhalo drops below the value of the average flux at the anticenter. The results may depend on the actual number of individual subhalos in the Monte Carlo simulations. To check the robustness of the results, the authors of [40] have performed a number of convergence tests in which they demonstrated that increasing the number of individual halos does not change the estimate of their detectability. The scatter among the results is obtained from the different Monte Carlo realizations of the subhalo population.

Finally, to compute the extragalactic contribution to the annihilation flux, we have used the formalism of [76], modified as in Sec. VI C of [17], in order to account for the mass and radial dependence of the subhalo concentrations.

Figure 4 shows the predicted contribution of the smooth MW halo, MW subhalos, and extragalactic halos to the γ-ray flux from DM annihilation integrated above 3 GeV, as a function of the angle of view ψ from the GC, in the case of *Aquarius* and *Via Lactea II*, respectively. The contribution from individual subhalos is computed by averaging over the 10 Monte Carlo realizations.

In the central part, the annihilation signal is dominated by the MW smooth component in both *Aquarius* (at $\psi < 50°$) and *Via Lactea II* (at $\psi < 20°$). Away from the GC, the dominant contribution is provided by DM subhalos in the *Via Lactea II* case and by extragalactic background in the *Aquarius* case. The different behaviors simply reflect

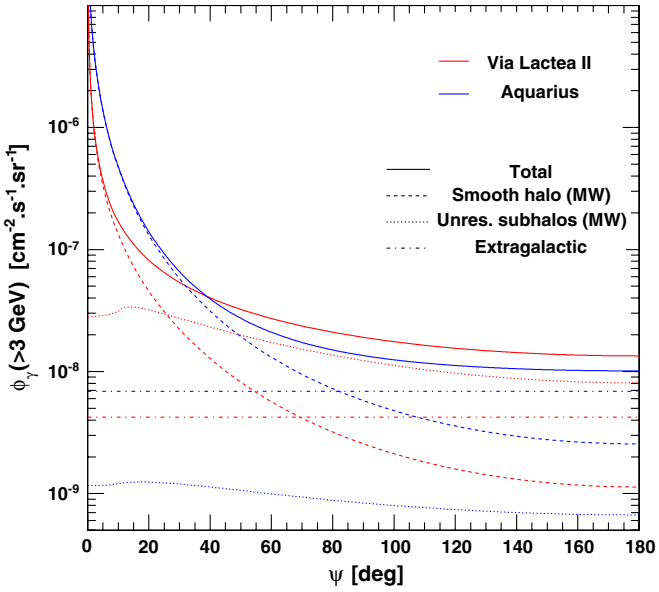

FIG. 4 (color online). Contribution to the γ-ray flux from DM annihilation, as a function of the angle of view from the GC, of the MW smooth (dashed curves), MW subhalo (dotted curves), and extragalactic (dotted-dashed curves) components for the *Aquarius* (blue, dark gray lines) and *Via Lactea II* (red, light gray lines) setup. The plain curves show the total contribution for each configuration. Fluxes are measured over a solid angle of 10^{-5} sr.

our choice of extrapolation below the simulations' resolution limit.

We note that our predictions satisfy the observational constraint represented by the diffuse Galactic signal. Indeed, the *mean* diffuse Galactic flux above 3 GeV that should be measured by Fermi ($\sim 5.3 \times 10^{-7}$ ph cm^{-2} s^{-1} sr^{-1}) is safely above the expected annihilation signal in both simulation setups.

The flux in the innermost regions is higher for the *Aquarius* simulation, as is clear from the full-sky maps shown in Fig. 5, where we show the total annihilation flux (MW smooth + Galactic subhalos + extragalactic halos and subhalos). The fact that the annihilation signal at the GC is higher in the *Aquarius* case is mostly because, in this simulation, the DM density in the solar neighborhood is larger than in *Via Lactea II*. This fact propagates in a mismatch between the two fluxes proportional to the density squared, i.e., $[\rho_{\rm sm}^{Aq}(\odot)/\rho_{\rm sm}^{VLII}(\odot)]^2 = [0.57/0.42]^2 = 1.84$. An additional source of discrepancy is the fact that the total mass of the MW in the *Via Lactea II* simulation is smaller than in *Aquarius*, as reported in Table I. However, as shown in Fig. 6, the two predictions can be brought to

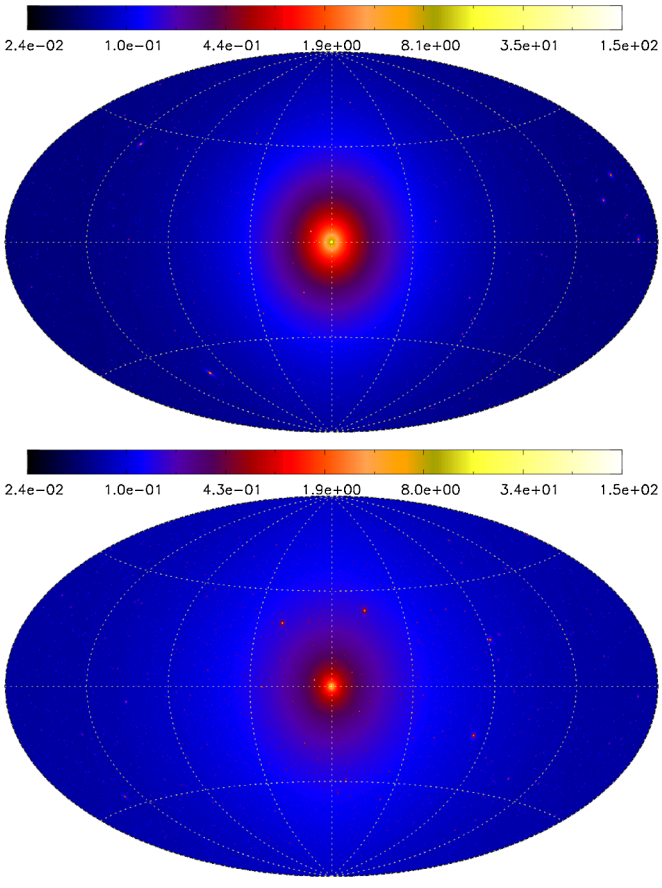

FIG. 5 (color online). Full-sky map, in Galactic coordinates, of the number of photons (above 3 GeV) produced by DM annihilation (benchmark A). The top (bottom) panel shows the predicted flux in the *Aquarius* (*Via Lactea II*) setup.

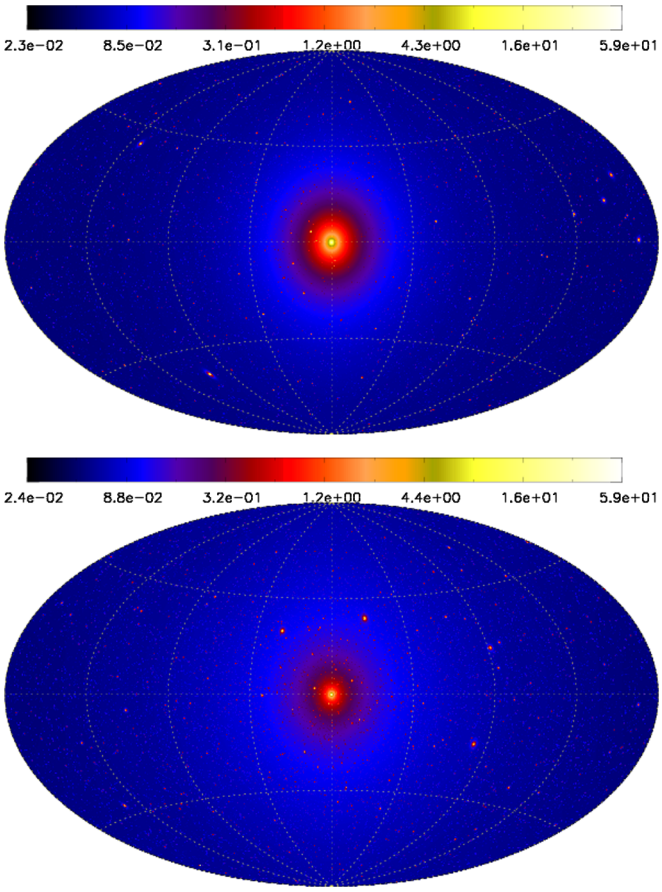

FIG. 6 (color online). Same as Fig. 5, but with the two simulation setups rescaled to the same local density, same total mass, and same fraction of mass in substructures.

agreement by requiring that (i) both *Via Lactea II* and *Aquarius* have the same local density $\rho_\odot$ (we have taken the recent estimate $\rho_\odot = 0.385$ GeV/cm^3 from [77,78]), (ii) the same subhalo mass fraction ($f_{\rm sub}^{\rm tot} = 0.18$) is adopted, and (iii) the same mass profile is assumed.

A. Experimental detectability

In order to assess the detectability of the γ-ray annihilation flux with the Fermi-LAT satellite, we have to specify what the signal, background, or noise are.

If we are interested in finding a signal above the astrophysical backgrounds, the signal is contributed by the sum of all the aforementioned components of the annihilation flux (MW smooth mass distribution + Galactic subhalos + extragalactic halos and subhalos). We focus on photons with energies larger than 3 GeV and we assume an exposure time of 1 yr, which corresponds to about 5 years of data-taking with Fermi, and we assume an effective detection area of 10^4 cm^2. We do not consider here any dependence on the photon energy nor on the incidence angle. The background or noise is contributed by the diffuse Galactic foreground and the unresolved extragalactic background. As mentioned in Sec. I, to model such contributions we

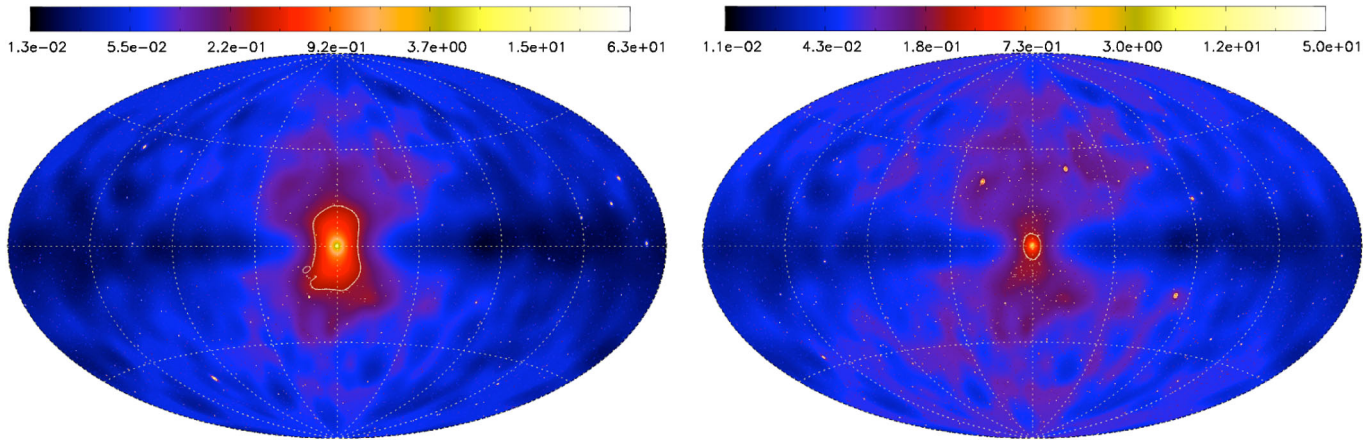

FIG. 7 (color online). Sensitivity map, in Galactic coordinates, for the *Aquarius* and *Via Lactea II* setups. The signal is as in Fig. 5, while the background is obtained through a suitable rescaling of the EGRET maps (see text for further details).

have rescaled the EGRET data at $E > 3$ GeV by 50%. We remind that this reduction reflects the fact that the Fermi data do not confirm the so-called Galactic excess measured by EGRET. The expected sensitivity is simply given by $\sigma_{\rm DM} = \frac{N^{\gamma}_{\rm DM}}{\sqrt{N^{\gamma}_{\rm background}+N^{\gamma}_{\rm DM}}}$, where $N^{\gamma}_{\rm DM}$ is the total number of annihilation photons, and $N^{\gamma}_{\rm background}$ are the photons contributed by the astrophysical background. The left and right panels of Fig. 7 show the resulting sensitivity maps in Galactic coordinates for the *Via Lactea II* and the *Aquarius* simulations, respectively. The sensitivity maps have a sharp peak near the GC, as expected. Isosensitivity contours are not symmetric but have a characteristic 8-shape around the GC due to the disklike astrophysical Galactic foreground that contributes to the noise term. It is worth noticing that point sources have not been included in this signal-to-noise calculation. Their inclusion would strongly lower the sensitivity of the Galactic center region. The sensitivity maps after the rescaling procedure adopted to produce the two maps in Fig. 6 would look very similar to the left panel of Fig. 7.

This procedure can be useful to estimate the regions that optimize the signal-to-noise in DM searches. In fact, while the Fermi data become available, one can just take the DM template presented here and divide the actual Fermi data by such a template. One can, then, calculate the signal-to-noise ratio, S/N, for the isoflux contours, and determine the size and the shape of the region that maximizes the S/N.

Disentangling the annihilation signal from the astrophysical one near the GC might, however, be difficult due to the presence of a strong astrophysical background. An alternative strategy is to look for individual subhalos, i.e., isolated bright spots in the γ-ray sky. In this case, the signal is given by the annihilation photons produced in the nearest and γ-ray brightest subhalos in our Monte Carlo realizations. The noise is contributed by all remaining sources of γ-ray photons, including those from DM annihilation (MW smooth + average subhalo component + extragalactic). The sensitivity is, in this case, given by $\sigma_h = \frac{N^{\gamma}_{\rm signal}}{\sqrt{N^{\gamma}_{\rm back+fore}}}$, where $N^{\gamma}_{\rm signal} = N^{\gamma}_{\rm subhalos,\ MC}$ are the annihilation photons produced within the resolved subhalos, and $N^{\gamma}_{\rm back+fore} = N^{\gamma}_{\rm MW,\ smooth} + N^{\gamma}_{\rm subhalos,\ average} + N^{\gamma}_{\rm extragalactic} + N^{\gamma}_{\rm background}$ includes contributions from the smooth MW halo, unresolved subhalos, diffuse extragalactic background, and the Galactic foreground, respectively.

In Table IV, we list the number of 3σ and 5σ detections expected with an exposure of 1 yr with the Fermi-LAT. Both the *Aquarius* and the *Via Lactea II* cases are considered. The number of detectable subhalos is small but significantly different from zero in benchmark models A and B. No individual subhalos are expected to be detected in the case of models C and D.

Figure 8 shows the number of subhalos detectable at 3σ for the benchmark model A, as a function of the subhalo mass. The symbols and error bars represent the mean and the scatter over the 10 Monte Carlo realizations. All detectable subhalos have masses above $10^5 M_{\odot}$, in some cases comparable to the estimated masses of the local dwarf galaxies, suggesting that these DM-dominated objects may, indeed, be good targets for DM indirect detections. Furthermore, the results show that the only detectable halos are those already resolved in the *Aquarius* and *Via Lactea II* simulations, i.e., the results presented here are

TABLE IV. Number of subhalos detectable at 3 and 5σ with the Fermi-LAT satellite in 5 years of data-taking, computed for the benchmark models A and B. Errors represent the scatter over 10 Monte Carlo realizations.

Model	*VLII* 3σ	*VLII* 5σ	*Aq* 3σ	*Aq* 5σ
A	9.2 ± 2.6	4.1 ± 1.3	13.5 ± 2.5	7.3 ± 2.4
B	3.1 ± 1.1	1.4 ± 0.8	6.2 ± 2.1	2.9 ± 1.4

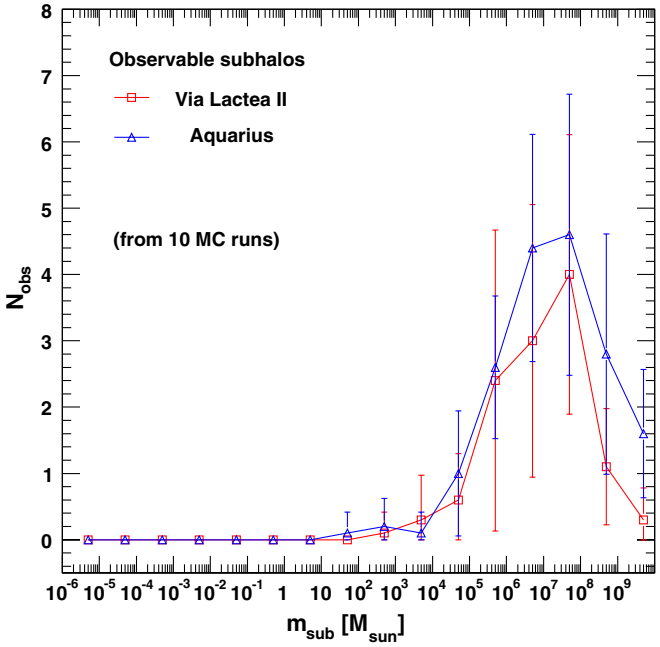

FIG. 8 (color online). Number of halos that can be detected at 3σ with an exposure of 1 yr on-axis (corresponding to approximately 5 years of data taking) with the Fermi-LAT, in the case of the *Via Lactea II* and *Aquarius* simulations and the particle physics benchmark model A, as a function of the halo mass. Errors represent the scatter over 10 Monte Carlo realizations.

independent of the aggressive extrapolations required to model the properties of low-mass subhalos.

V. ANTIMATTER

Antimatter cosmic rays (CRs) have long been considered as potential tracers of DM annihilation because they are barely produced in standard astrophysical processes [79]. Indeed, most of the standard contributions are expected to be of secondary origin, i.e., produced by nuclear interactions of standard CRs (protons and light nuclei) with interstellar gas (hydrogen and helium). This picture is essentially true for antiprotons because their propagation scale is rather large compared to the spatial fluctuations of the interstellar medium and CR sources, but should be taken with caution for positrons, since their high-energy component is strongly sensitive to time and spatial fluctuations of the local environment. Moreover, some astrophysical sources, like pulsars, are known to have the capability to produce positrons from pair creations in strong magnetic fields (see an early discussion on this in [80]). Because there are such sources in abundance within the kpc scale around the Earth, one can expect them to be significant contributors to the high-energy positron budget [7,12]. Nevertheless, many theoretical as well as observational uncertainties still affect the modeling of most astrophysical sources [12]. It is, consequently, important to scrutinize the potential imprints that DM annihilation could provide in the antimatter budget, in addition to those in γ rays. In this section, we will shortly review the transport of CRs in the Galaxy and then focus on the positron and antiproton fluxes at Earth that DM annihilation may generate. To model the sources of the annihilation products, we will again use the highest-resolution N-body simulations discussed in the previous sections, including the effect of subhalos. For more details on the semianalytical method used to follow the antimatter transport within the Galaxy that will be used in the following, we refer the reader to [59,72].

A. High-energy positron and antiproton transport

Antimatter CRs in the GeV–TeV energy range, like other charged cosmic rays, diffuse on the inhomogeneities of the Galactic magnetic field. Because those inhomogeneities are not fully confined in the Galactic disk, cosmic rays can pervade beyond this tiny region and diffuse away up to a few kpc upwards and downwards (see, e.g., [81] for a pedagogical insight). This turbulent volume actually defines the diffusion zone inside which CRs are confined and beyond which they escape forever; it can be featured as a disklike slab with radial and vertical extensions, $R_{\rm slab}$ and L, respectively. In the following, we will fix $R_{\rm slab} = 20$ kpc, and $L = 4$ kpc [82]. CRs experience different processes during their journey, depending on their nature: in addition to spatial diffusion, (anti)nuclei will be mostly affected by convection and spallation in the interstellar medium localized in the disk, processes which are more efficient at low energy, while electrons and positrons will have their transport dominated by energy losses above a few GeV. Formally, given a source $\mathcal{Q}$, all CRs obey the same continuity equation [83],

$$\hat{\mathcal{D}}\hat{\mathcal{J}} = \partial_\mu \mathcal{J}^\mu + \partial_E \mathcal{J}^E + \Gamma \mathcal{N} = \mathcal{Q}(\vec{x}, E, t), \qquad (17)$$

where $\mathcal{N} = dn/dE$ is the CR density per energy unit, $\mathcal{J}^\mu$ is the space-time current, $\mathcal{J}^E$ the energy current, and Γ stands for a destruction rate (spallation for nuclei). The time current is merely the CR density $\mathcal{J}^t \equiv \mathcal{N}$, while the spatial current is reminiscent of the Fick law and accounts for the spatial diffusion and convection $\mathcal{J}^{\vec{x}} \equiv \{K_x(\mathcal{R})\vec{\nabla} - \vec{V}_c\}\mathcal{N}$. The spatial diffusion coefficient, describing the stochastic bouncing interactions with the magnetic inhomogeneities, is usually parametrized as $K_x(\mathcal{R}) = K_0(\mathcal{R}/1\ \mathrm{GV})^\delta$, where the dependence on the CR rigidity $\mathcal{R} \equiv p/Z$ is explicit. The energy current carries the energy-loss and reacceleration terms $\mathcal{J}^E \equiv \{dE/dt - K_p(E)\partial_E\}\mathcal{N}$.

Although all CR species obey the same transport equation, some of the processes mentioned above will be negligible in the GeV–TeV energy range, depending on the species. Beside spatial diffusion, antiprotons will mostly suffer spallations and convection, but almost never energy losses. On the contrary, energy losses will dominate

the positron transport, mainly due to the inverse Compton scattering with the CMB photons and the interstellar radiation fields and to synchrotron losses with the Galactic magnetic field. In both cases, reacceleration is negligible above a few GeV [64,82]. Neglecting the irrelevant terms and assuming a steady state ($\partial_t \mathcal{N} = 0$), the Green functions—or propagators—associated with the transport equation can be derived analytically for antiprotons and positrons. We refer the reader to [72] for the detailed expressions of the propagators. In the following, $\mathcal{G}$ will denote the Green function, such that $\hat{\mathcal{D}}\mathcal{G}(\vec{x}, E \leftarrow \vec{x}_S, E_S) = \delta^3(\vec{x} - \vec{x}_S)\delta(E - E_S)$, where S indexes the source quantity. More details on CR propagation can be found in, e.g., [81,83–86].

Most of the propagation parameters can be constrained from measurements of the ratios of secondary to parent primary species, and we will use the *median* set derived in [87]: $K_0 = 1.12 \times 10^{-2}$ kpc^2 Myr^{-1}, $\delta = 0.7$, and $V_c = 12$ km/s. The energy-loss rate ascribed to positrons will be $dE/dt = -b(E) = -b_0 E^2$, with $b_0 = (\tau_{\rm loss} \times 1\,{\rm GeV})^{-1} = 10^{-16}\,{\rm s}^{-1}\,{\rm GeV}^{-1}$, which is a reasonable approximation accounting for the inverse Compton loss on CMB, starlight and dust radiation, and for the synchrotron loss [64,81,88]. However, we remind that there are theoretical uncertainties and degeneracies among those propagation parameters [82], so that predictions for primaries and secondaries may vary by large factors (see [87] for primary antiprotons and [72,89] for primary positrons).

An important consequence of the differences in the propagation histories among species is that the corresponding characteristic propagation scales also differ. For antiprotons, the propagation scale is set by the spatial current, $\lambda_{\bar{p}} = K(\mathcal{R})/V_c \sim 1(T/{\rm GeV})^{\delta}$ kpc, and increases with energy. At variance with antiprotons, positrons have their propagation scale set by transport in both space and momentum, $\lambda_{e^+} \propto \{\int dE K(E)/b(E)\}^{1/2}$, which roughly scales like $\sim 3(E/{\rm GeV})^{(\delta-1)/2}$ kpc for a loss of half the injected energy. Therefore, the positron range decreases with energy (see, e.g., Fig. 2 of [90]). Consequently, low-energy antiprotons and high-energy positrons observed at Earth must originate from the very local environment. For instance, a positron injected in the Galaxy at 200 GeV and detected at 100 GeV has a probability to originate from regions farther than $\sim$1.5 kpc from the observer, which is Gaussianly suppressed.

Besides the primary signals due to DM annihilation that we will discuss below, one should also be aware of the backgrounds and their theoretical uncertainties. Since we disregard, here, the conventional astrophysical sources of CRs, our positron and antiproton backgrounds are those secondaries resulting from the spallation processes of cosmic protons and nuclei with the interstellar matter located in the disk. We refer the reader to [63,64] for thorough discussions on those secondary components and related theoretical uncertainties. Throughout the paper, we will use the median secondary backgrounds derived in those references.

B. Smooth and clumpy DM contributions: boost factors

The fact that the DM spatial distribution is not smooth but actually fluctuates due to the presence of subhalos leads to local fluctuations in the annihilation rate [91]. Formally, any flux estimated from a smoothly averaged DM profile should, therefore, be enhanced by a factor $\langle \rho^2_{\rm dm} \rangle_{V_{\rm cr}} / \langle \rho_{\rm dm} \rangle^2_{V_{\rm cr}}$ to account for those fluctuations, the average being performed in a volume $V_{\rm cr}$ that depends on the CR propagation scale. Such an enhancement must be, therefore, quite different from what has been previously discussed for γ rays, simply because the averaging volume for the latter is the resolution cone carried by the line of sight instead of a propagation volume.

The antimatter flux at the Earth originating from the annihilation of a single, smoothly distributed DM component is given by the following expression:

$$\phi_{\rm sm}(E) = \frac{\beta c}{4\pi} \mathcal{S} \int_{\rm slab} d^3\vec{x}_S \tilde{\mathcal{G}}(\vec{x}_\odot \leftarrow \vec{x}_S, E) \left(\frac{\rho(r)}{\rho_\odot} \right)^2, \quad (18)$$

where $\tilde{\mathcal{G}}$ is the convolution of the Green function $\mathcal{G}(E \leftarrow E_s)$, with the injected spectrum dN/dE_S, $\mathcal{S} \equiv (\langle \sigma v \rangle/2)(\rho_\odot/m_\chi)^2$, and $\rho_\odot \equiv \rho_{\rm tot}(\vec{x}_\odot)$ is the DM density near the Sun inferred from the smooth profile $\rho_{\rm tot}$ in Eqs. (1) and (2).

Besides, we need to determine the average contribution due to the population of subhalos. The overall mass-density profiles of subhalos given by Eqs. (4) and (5) can be used to obtain the corresponding normalized probability function as follows:

$$\frac{d\rho_{\rm sh}(M_{\rm sub}, R)}{dM_{\rm sub}} = N^{\rm tot}_{\rm sub} \langle M_{\rm sub} \rangle \frac{d\mathcal{P}_V(R)}{dV} \frac{d\mathcal{P}_m(M_{\rm sub}, R)}{dM_{\rm sub}} = M^{\rm tot}_{\rm sub} \frac{d\mathcal{P}_V(R)}{dV} \frac{d\mathcal{P}_m(M_{\rm sub}, R)}{dM_{\rm sub}}, \quad (19)$$

where $N^{\rm tot}_{\rm sub}$ is the total number of subhalos, and $\langle M_{\rm sub} \rangle$ their mean mass. This expression is such that the product of $d\mathcal{P}$'s corresponds to a normalized probability function

$$\int d\mathcal{P}_{\rm tot} = \int_{\rm MW} d^3\vec{x} \frac{d\mathcal{P}_V(R)}{dV} \int_{m_{\rm min}}^{m_{\rm max}} dm \frac{d\mathcal{P}_m(m, R)}{dm} = 1. \quad (20)$$

Defining such a probability function allows us to treat each quantity related to a single subhalo as a stochastic variable [59]. Notice that, although the upper bound in the integral of the mass distribution is fixed to $m_{\rm max}$, the mass distribution itself is, in fact, a function of R. Such a dependence arises because of the tidal disruption of subhalos that is implemented in the present analysis according to the Roche criterion [see Eq. (10)] that we have discussed in Sec. II.

Before inferring the overall subhalo flux, we need to define the luminosity of a single object. Given a subhalo of inner profile $\rho_{\rm sub}^{\rm DM}$, the corresponding annihilation rate will be proportional to the *annihilation volume*

$$\xi_{\rm sub}(M_{\rm sub},R)\equiv 4\pi\int_{V_{\rm sub}} dr r^2\left[\frac{\rho_{\rm sub}^{\rm DM}(r,M_{\rm sub},R)}{\rho_\odot}\right]^2, \quad (21)$$

which is the volume that would be necessary to obtain the whole subhalo luminosity from the local DM density $\rho_\odot=\rho_{\rm tot}(\odot)$ associated with the DM setup of interest. As detailed in previous sections, the concentration parameter $c(M_{\rm sub},R)$, which characterizes the shape of the inner density profile, depends on the subhalo mass $M_{\rm sub}$ and position R in the Galaxy.

Therefore, the CR flux for a subhalo population reads

$$\begin{aligned}\phi_{\rm sub}^{\rm tot}(E)&=\frac{\beta c}{4\pi}\mathcal{S}N_{\rm sub}^{\rm tot}\int_{\rm slab} d^3\vec{x}_s\tilde{\mathcal{G}}(\vec{x}_S,E)\frac{d\mathcal{P}_V(R)}{dV}\\&\quad\times\int_{m_{\rm min}}^{m_{\rm max}} dm\xi_{\rm sub}(m,R)\frac{d\mathcal{P}_m(m,R)}{dm}\\&=\frac{\beta c}{4\pi}\mathcal{S}N_{\rm sub}^{\rm tot}\int_{\rm slab} d^3\vec{x}_s\tilde{\mathcal{G}}(\vec{x}_S,E)\frac{d\mathcal{P}_V(R)}{dV}\langle\xi_{\rm sub}\rangle_{M_{\rm sub}}(R)\\&=\frac{\beta c}{4\pi}\mathcal{S}N_{\rm sub}^{\rm tot}\langle\tilde{\mathcal{G}}(\vec{x}_S,E)\langle\xi_{\rm sub}\rangle_{M_{\rm sub}}(R)\rangle_{\rm slab}=N_{\rm sub}^{\rm tot}\langle\phi_{\rm sub}\rangle.\end{aligned} \quad (22)$$

$\langle x\rangle_{m/V}$ means an average of the variable x according to the mass/spatial distribution, respectively. By writing this equation, we made the implicit assumption that a subhalo can be treated as a stochastic pointlike source. This assumption is valid while the typical propagation scale is larger than the scale radius of any subhalo, which is fully the case here: in the *Aquarius* setup, a $10^{-6}/10^6 M_\odot$ subhalo has a scale radius of $\sim 10^{-6}/3\times 10^{-2}$ kpc, respectively. We obviously recover the same result as in [72] that the total subhalo flux is given by the total number of subhalos times the mean flux from a single subhalo, consistently with the stochastic treatment. Nonetheless, the spatial average can no longer be separated from the mass average in the present study. Not only does this come from the full implementation of the tidal effects, but also from the spatial dependence of the concentration parameter (the two effects are related). Consequently, the average luminosity of a subhalo, $\langle\xi_{\rm sub}\rangle_{M_{\rm sub}}$, does explicitly depend on its location in the Galaxy, even when the spatial disruption à la Roche is neglected. We illustrate the radial dependence of $\langle\xi_{\rm sub}\rangle_{M_{\rm sub}}(R)$ in Fig. 9, where we explicitly show the effect of the tidal disruption: the average luminosity of a subhalo is quickly turned off in the central part of the Galaxy when the Roche criterion is applied.

Because the flux derived above is, in fact, a mean quantity, it can be associated with a statistical variance. Taking the single subhalo flux as a stochastic quantity, i.e., assuming subhalos are not spatially correlated, the relative

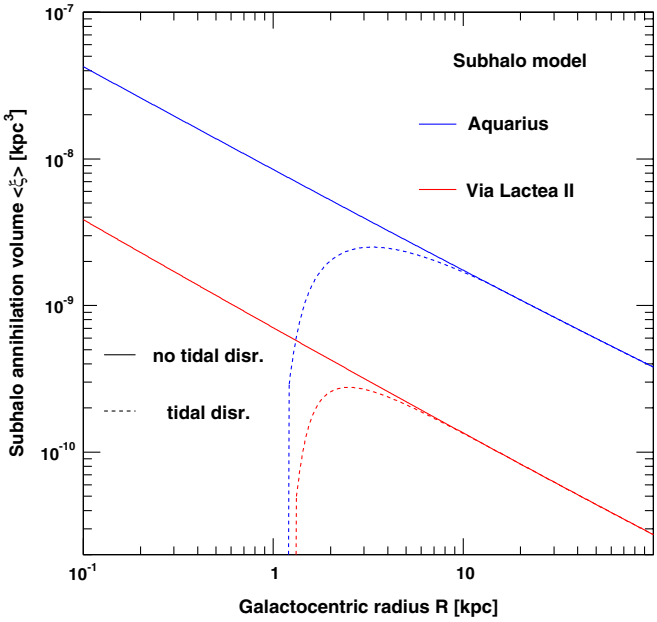

FIG. 9 (color online). Mean value of the subhalo annihilation volume $\langle\xi\rangle$ defined in Eq. (21) as a function of the galactocentric radius R. The solid/dashed curves show the effects of unplugging/plugging the subhalo tidal disruption for both the *Via Lactea II* (red, light gray lines) and *Aquarius* (blue, dark gray lines) configurations. For the sake of comparison, we have used $\rho_\odot=0.3$ GeV/cm^3 in Eq. (21) for both configurations.

fluctuation of the antimatter CR flux is given from Poissonian statistics in [59]:

$$\begin{aligned}\frac{\sigma_{\rm sub}^{\rm tot}}{\phi_{\rm sub}^{\rm tot}}(E)&=\frac{1}{\sqrt{N_{\rm sub}^{\rm tot}}}\frac{\sigma_{\rm sub}}{\langle\phi_{\rm sub}\rangle}(E)\\&=\frac{1}{\sqrt{N_{\rm sub}^{\rm tot}}}\left\{\frac{\langle\tilde{\mathcal{G}}^2(\vec{x}_S,E)\langle\xi_{\rm sub}^2\rangle_{M_{\rm sub}}(R)\rangle_{\rm slab}}{\langle\tilde{\mathcal{G}}(\vec{x}_S,E)\langle\xi_{\rm sub}\rangle_{M_{\rm sub}}(R)\rangle_{\rm slab}^2}-1\right\}^{1/2}.\end{aligned} \quad (23)$$

This quantity, associated with the whole population of subhalos, is linked to the fluctuation of the flux of a single object in a standard manner, with the factor $1/\sqrt{N}$. A large value would express the fact that a small number of subhalos may have a large impact on the predictions, while a small value ensures that the predictions are typified by contributions of a large number of objects. The relative fluctuation obviously increases with a decreasing propagation horizon, i.e., with increasing (decreasing) energy for antiprotons (positrons, respectively) [72]. It is important to stress that, for positrons, the quantity $\langle\tilde{\mathcal{G}}^2\rangle/\langle\tilde{\mathcal{G}}\rangle^2$ does actually diverge like $1/\lambda^3$ in the limit of a vanishingly small propagation scale (i.e., $E\to E_S$). Although this affects an infinitely small part of the propagated spectrum in the case of an injected positron line, this divergence spreads over the whole propagated spectrum in the case of the injection of positrons at all energies below m_χ. This

divergence would have a physical meaning if there was a nonzero probability that a subhalo were located exactly at the positron detector, which is obviously not the case. To avoid this calculation artefact, we conservatively assume that there is no DM source fluctuation within 50 pc around the Earth, which prevents any computation crash.

The overall antimatter CR flux is the sum of the subhalo component plus the smooth component, the latter being somewhat corrected for not carrying the whole DM mass anymore: $\phi_{\rm tot} = \phi_{\rm sm} + \phi^{\rm tot}_{\rm sub}$, which is not expected to equal $\bar{\phi}_{\rm tot}$, i.e., the flux computed from the overall smooth halo featured by Eq. (1) or (2). The so-called boost factor is, then, merely defined from their ratio

$$\mathcal{B}(E) = \frac{\phi_{\rm tot}}{\bar{\phi}_{\rm tot}} \approx 1 + \frac{\phi^{\rm tot}_{\rm sub}(E)}{\phi_{\rm sm}(E)}, \tag{24}$$

where we have used $\phi_{\rm sm} \approx \bar{\phi}_{\rm tot}$ in the latest approximation. We emphasize that the boost factor does depend on energy. The smooth component will dominate at a large propagation scale, when the dense regions close to the Galactic center come into play. On the contrary, the contribution of subhalos may be significant at small propagation scales, because the smooth contribution is set by the squared local DM density. There is a close parallel to make with the boost factor as computed for γ rays, for which the relevant physical variable is not the energy, but the angle between the line of sight and the Galactic center direction ψ: the boost is negligible at small angles because of the large contribution of the central part of the Galaxy. Finally, note that $\mathcal{B}(E)$ also depends on the injection spectrum for positrons because of energy losses. This is not the case for antiprotons, although their associated boost factor still depends on the energy because of spatial diffusion.

The boost factor is associated with a statistical fluctuation that is straightforwardly connected to that of the total subhalo flux:

$$\sigma_{\mathcal{B}}(E) = \frac{\sigma^{\rm tot}_{\rm sub}(E)}{\bar{\phi}_{\rm tot}(E)}. \tag{25}$$

We see that, even if fluctuations of the subhalo flux were found to be large compared to the subhalo flux itself, the boost factor would have a sizable variance only if those fluctuations are greater than the smooth flux. This mostly characterizes the large propagation scale regime, where the smooth contribution can strongly dominate the signal and completely overcome the statistical variance expected from the subhalo flux.

It turns out to be possible to derive an analytical expression for the boost factor, or equivalently for the total subhalo flux, in the vanishingly small propagation scale limit [72]. This asymptotic expression is very convenient not only to check numerical computations, but also because it usually corresponds to the maximal mean value of the boost factor—which can, of course, fluctuate around its mean value. This analytical limit relies on the fact that, at a very short propagation scale, the Green function $\mathcal{G}(\vec{x}_\odot \leftarrow \vec{x}) \to^{\propto} \delta(\vec{x} - \vec{x}_\odot)$, so that $\tilde{\mathcal{G}} \to^{\propto} \delta(\vec{x} - \vec{x}_\odot)\frac{dN}{dE}$. We are, therefore, left with local quantities:

$$\begin{aligned}\mathcal{B}_\odot &= \left[\frac{\rho_{\rm sm}(R_\odot)}{\rho_{\rm tot}(R_\odot)}\right]^2 + N^{\rm tot}_{\rm sub}\langle\xi_{\rm sub}(R_\odot)\rangle\frac{d\mathcal{P}_V(R_\odot)}{dV} \\ &\simeq 1 + N^{\rm tot}_{\rm sub}\langle\xi_{\rm sub}(R_\odot)\rangle\frac{d\mathcal{P}_V(R_\odot)}{dV}.\end{aligned} \tag{26}$$

We emphasize that this expression is valid for *any* CR species and for *any* set of propagation parameters, in the regime of a vanishingly small propagation scale. Nevertheless, we also remind that such a regime is generally associated with large statistical fluctuations of the boost factor, because the average number of subhalos in such a small volume can be of the order of unity or less: the actual boost can be much larger if we sit on the top of a subhalo, or much lower if no bright object wanders in the neighborhood.

C. Benchmark results and discussion

In this section, we discuss the results we have obtained for the overall positron and antiproton fluxes and corresponding boost factors, using the benchmark weakly interacting massive particles (WIMPs) defined in Sec. III and the DM distributions associated with the *Via Lactea II* and *Aquarius* configurations.

1. Boost factors

In Fig. 10, we show the results obtained for the boost factors and the corresponding 1-σ statistical bands, for both the positron and the antiproton signals.

The left panel of Fig. 10 represents the boost factor as a function of the positron energy given at different DM distributions (*Via Lactea II*- or *Aquarius*-like) and assumes the injection of a 100 GeV positron line at the source. The *Via Lactea II* subhalo configuration is shown to have much more impact than the *Aquarius* one, although the averaged boost factor is still modest, reaching a value of $\sim$3 asymptotically. The subhalo contribution has little effect in the *Aquarius* setup, except from the related statistical fluctuations at high energy [colored (shaded) areas]. These fluctuations size the probability that a nearby (or few) massive subhalo dominates the signal. The dashed curves illustrate the effect of applying the Roche disruption in the central region of the Galaxy. Since it is mostly efficient in the inner 2 kpc of the Galaxy (see Fig. 1), the effect is almost negligible in terms of the averaged boost factor, as expected. Nevertheless, the variance is strongly depleted [from the colored (shaded) to the hatched areas], due to a significant decrease of the fluctuations related to ξ in Eq. (23). Indeed, the available mass range is locally squeezed down when the Roche criterion is applied, as shown in Fig. 2; likewise, tidal disruption is most effective in the inner kpc of our Galaxy, where the bulk of subhalos is made by small objects and, therefore, preferentially

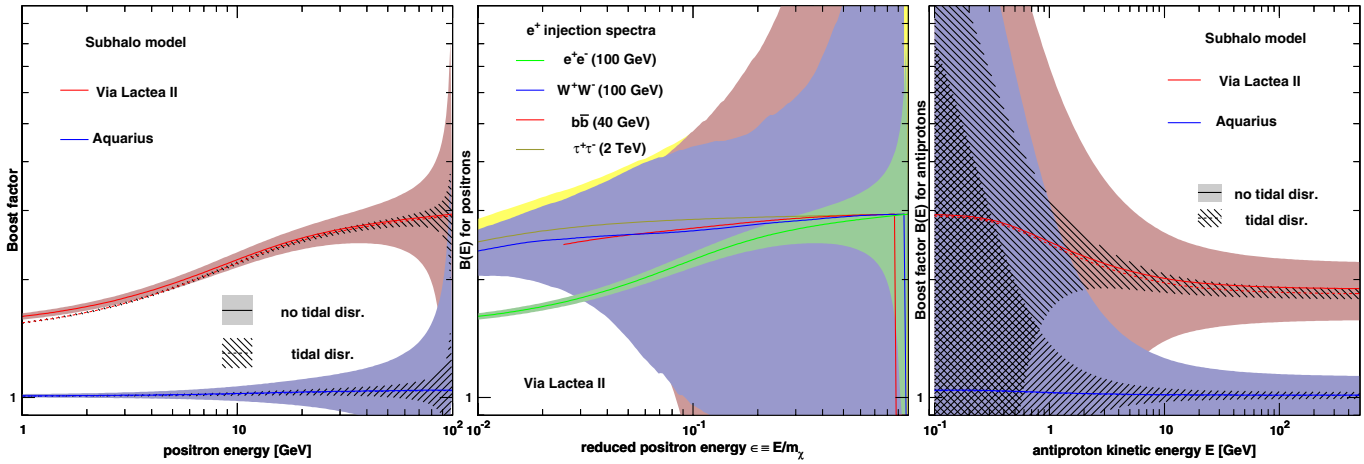

FIG. 10 (color online). Left: boost factor on positrons for different (sub)halo models, *Via Lactea II* (red, light gray lines) and *Aquarius* (blue, dark gray lines), assuming a 100 GeV positron line injected at the source. Middle: boost for positrons for different injected spectra and for the *Via Lactea II* case. Right: boost for antiprotons and for the same (sub)halo modes as in the left panel. All boosts are computed without solar modulation; colored (shaded) bands account for a 1σ fluctuation, which shrink to the hatched areas once the Roche criterion is plugged.

affects those substructures that are more concentrated (see Fig. 9).

The middle panel of Fig. 10 shows the boost factors for the positron fluxes associated with all our benchmark WIMP models (see Sec. III), the injection spectra of which differ significantly. These boost factors are computed in the frame of the *Via Lactea II* setup only and are plotted as functions of $x \equiv E/m_\chi$ for a more convenient reading. It is remarkable that the mean values converge towards the same limit at high energy, as expected from the short-range limit given in Eq. (26). The energy dependence of the averaged boost factor is a bit steeper in the case of a positron line because (i) the spatial origin of positrons at the Earth is more strongly connected to their energy in that case, so that the low-energy part mostly comes from the smooth GC component (instead, injection occurs at all energies $<m_\chi$ for a continuous spectrum, which alleviates this segregation as the spectrum gets softer); (ii) a given value of x corresponds to different energies and, therefore, to a different propagation scale, given the WIMP mass (especially relevant for the $\tau^+\tau^-$ model). The previous arguments also explain the more pronounced differences arising in the variance band shapes. Still, an additional point can help better understanding the differences in the variance shapes, which is inherent to continuous spectra. As mentioned below Eq. (23), the subhalo flux fluctuations are intrinsically divergent in the limit $E \longrightarrow E_S$: although made finite thanks to our spatial cutoff, they are still large and spread over the whole energy range in the case of continuous spectra (instead, they are confined around the monochromatic injection energy for the positron-line model).

Finally, the right panel of Fig. 10 exhibits the boost factors for antiprotons in the *Via Lactea II* and *Aquarius* configurations, which are independent of the injection spectra. We remark that the asymptotic value at low energy is the same as what is obtained for high-energy positrons (see left panel). This illustrates the validity of the asymptotic limit arising in the short propagation range regime and given in Eq. (26). Fluctuations are shown to be large at low energy, where convection and spallations are important; nevertheless, further accounting for solar modulation effects will be shown to deplete these large fluctuations significantly and shift them to much lower energies, irrelevant for measurements at the Earth.

2. Predictions of the antiproton and positron fluxes

We have computed the expected antimatter flux for all the benchmark WIMP candidates discussed in Sec. III. The results are shown in Figs. 11–13, where we have applied a force field of 600 MV to account for solar modulation. Figure 11 displays our full results for both the *Via Lactea II* and *Aquarius* configurations, Fig. 12 shows the effect of plugging the Roche disruption, and Fig. 13 is the same as Fig. 11 when the local dark matter density of both configurations is rescaled to $\rho_\odot = 0.385$ GeV cm^{-3}. In each figure, the left, middle, and right panels show the positron flux, the positron fraction, and the antiproton flux, respectively, with the associated 5σ fluctuations caused by the presence of subhalos; the plots in the upper (lower) row are those associated with the *Via Lactea II* (*Aquarius*) setup. The solid colored curves correspond to the mean values predicted for our benchmark WIMP models when subhalos are included (the colored bands encompass the 5σ contours), while the dashed colored curves are the expectations in the absence of subhalos. Our theoretical predictions are compared with the observational data taken from [92–94] for positron flux, from [1,95–97] for the positron fraction,

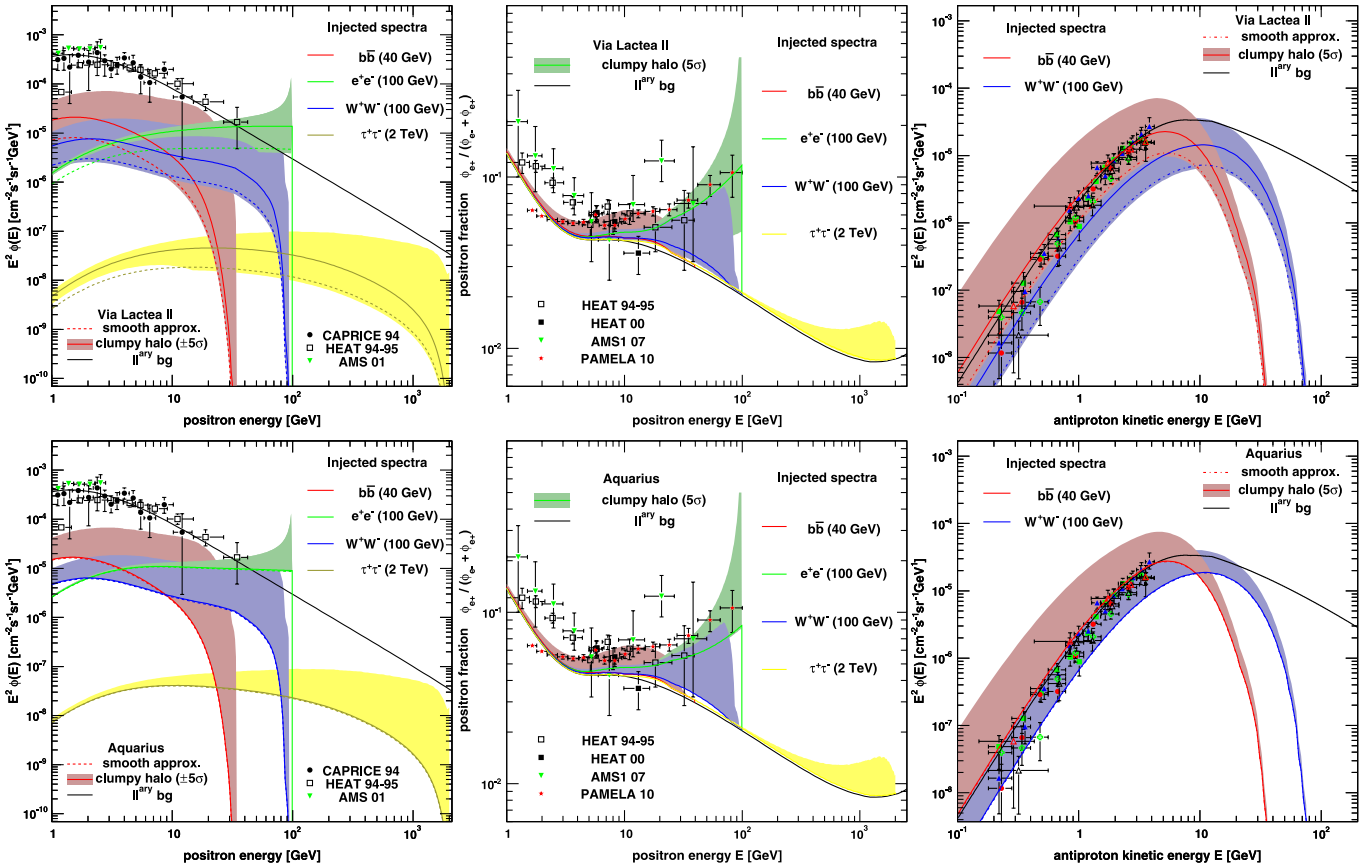

FIG. 11 (color online). Positron flux (left panel) and positron fraction (middle panel) for our benchmark WIMP models. Right: antiproton fluxes for the WIMP models annihilating into $b\bar{b}$ and W^+W^-. The top (bottom) row corresponds to the results obtained for the *Via Lactea II* (*Aquarius*) setup when the tidal disruption à la Roche is unplugged. The effects of tidal disruption are shown in Fig. 12.

and from [94,98–101] for the antiproton flux. We also report the secondary background flux predictions from [64] for positrons and from [63] for antiprotons.

Interestingly enough, we remark that the antiproton predictions provide rather tight constraints on our dark matter modeling (see right panels). Indeed, the averaged predictions obtained for the 40 GeV $b\bar{b}$ model are in tension with the data in both the *Via Lactea II* and *Aquarius* configurations (top right and top left panels, respectively). Additional contributions from subhalo fluctuations (5σ) are excluded since clearly overshooting the data, even when tidal disruption towards the Galactic center is implemented (see Fig. 12). The observational constraints are less severe for the 100 GeV W^+W^- model, the averaged predictions of which lie at a factor of $\sim$2 below the secondary prediction. Note, however, that large fluctuations above the mean predicted fluxes would again be in tension with the data, reaching the secondary background prediction when tidal effects are plugged (even exceeding it when they are neglected).

We have verified that the subhalos observable in γ rays, the coordinates and properties of which were extracted from our Monte Carlo runs, are not dominating the overall antiproton flux, as expected. Indeed, since the antiproton range is large at the GeV–TeV energy scale, the bulk of the antiproton flux does, in fact, originate mostly from the large population of unresolved subhalos at low and intermediate energies and from the Galactic central regions at higher energies (see the boost factor predictions in the right panel of Fig. 10). This means that, as soon as subhalos dominate the overall contribution, which is the case in the *Via Lactea II* configuration, rescaling the smooth dark matter density down would not be sufficient to decrease the predictions. The comparison of Fig. 11 with Fig. 13 is a rather striking illustration: predictions associated with the *Via Lactea II* setup are poorly affected by a rescaling of the smooth dark matter density, whereas those with the *Aquarius* setup are clearly decreased. Therefore, a *Via Lactea II*-like setup for subhalos (steep mass profile) associated with low WIMP mass models coupling to quarks seems clearly disfavored by the current data. Nevertheless, we should also keep in mind that cosmic-ray propagation is affected by large theoretical uncertainties, the impacts of which are much stronger on the dark matter yields than on the background predictions. For instance, lowering the vertical extent of the diffusion zone (and lowering the diffusion coefficient accordingly to fulfill the B/C constraints) or increasing the convection velocity would result

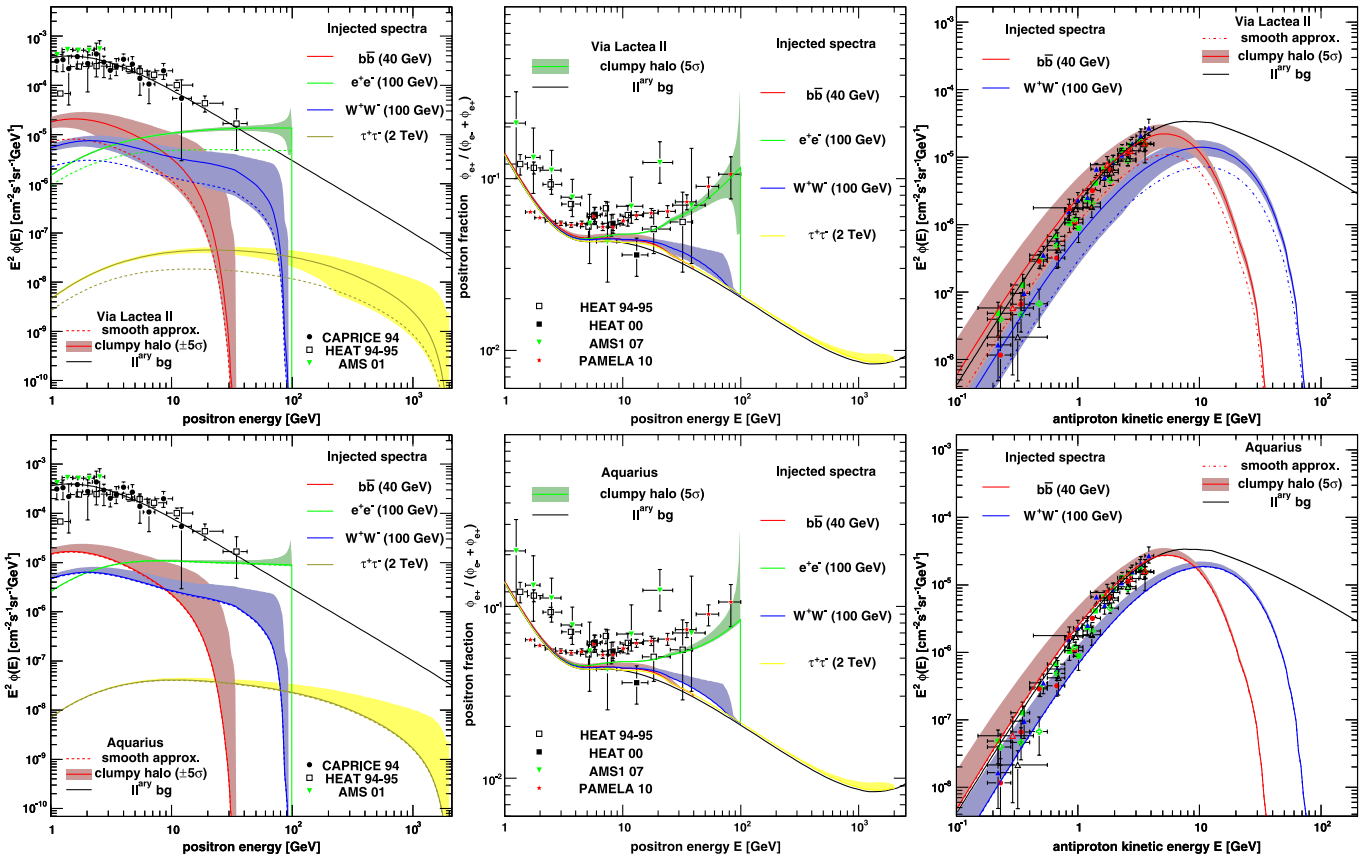

FIG. 12 (color online). Same as Fig. 11, but when plugging the Roche tidal disruption effects.

in lower flux predictions [87], which could rehabilitate such scenarios.

As regards the positron flux, it is interesting to note that the predicted mean fluxes are much lower than the secondary background expectation by $\sim$1 order of magnitude for all benchmark models but the one annihilating into electron-positron pairs. Disregarding this latter case for the moment, it turns out that 5σ statistical fluctuations could still lead to observational spectral features for the W^+W^- model, as made clearer in the positron fraction plots. Nevertheless, this statistical effect is actually cancelled as soon as tidal effects are implemented, as shown in Fig. 12. Indeed, the probability that a nearby single and very luminous subhalo (with typical mass $\gtrsim 10^{6-7} M_\odot$) dominates the overall flux is much smaller in that case (see the allowed maximal masses in Fig. 2). Note that, at variance with the antiproton signal, a single nearby object can dominate the high-energy flux in the case of positrons, due to their short propagation range.

Focusing on the 100 GeV positron-line model, we can further compare our two dark matter distribution configurations, for which the predictions generically exceed the secondary background. This can be understood easily by deriving the general analytical expression of the flux for an injected positron line in the limit $E \to m_\chi$, which reads for standard quantities:

$$\begin{aligned}\phi^\chi_{e^+}(E \to m_\chi) &= \frac{\delta \beta c}{4\pi} \frac{\tau_{\rm loss} E_0}{E^2} \frac{\langle \sigma v \rangle}{2} \left(\frac{\rho_\odot}{m_\chi}\right)^2 \\ &\approx 3 \times 10^{-10}\ {\rm cm}^{-2}\,{\rm s}^{-1}\,{\rm GeV}^{-1}\,{\rm sr}^{-1} \frac{\tau_{\rm loss}}{10^{16}\,{\rm s}} \\ &\times \left[\frac{\rho_\odot}{0.3\ {\rm GeV/cm}^3}\right]^2 \left[\frac{m_\chi}{100\ {\rm GeV}}\right]^{-4} \\ &\times \frac{\langle \sigma v \rangle}{3 \times 10^{-26}\ {\rm cm}^3/{\rm s}}. \end{aligned} \quad (27)$$

Surprisingly enough, it is exactly the value of the predicted background flux $\phi^{\rm bg}_{e^+}(E = 100\ {\rm GeV}) \approx 3 \times 10^{-10}\ {\rm cm}^{-2}\,{\rm s}^{-1}\,{\rm GeV}^{-1}\,{\rm sr}^{-1}$ at 100 GeV in the median model of [64]. This formula is readily applied to the *Via Lactea II* setup by using $\rho_\odot = 0.42\ {\rm GeV\,cm}^{-3}$ and multiplying by the local boost factor, which can be taken from Fig. 10. We find $\phi^\chi_{e^+}(m_\chi = 100\ {\rm GeV}) \approx 1.7 \times 10^{-9}\ {\rm cm}^{-2}\,{\rm s}^{-1}\,{\rm GeV}^{-1}\,{\rm sr}^{-1}$, which is larger than the secondary positron flux by a factor of $\sim$6. We note that this asymptotic flux prediction is only valid for $E \to m_\chi$ and falls, thereby, very quickly with m_χ like m_χ^{-4}. We will further comment on this when discussing the positron fraction in Sec. V C 3.

Finally, we stress again that the theoretical uncertainties on the propagation parameters are still large, and the

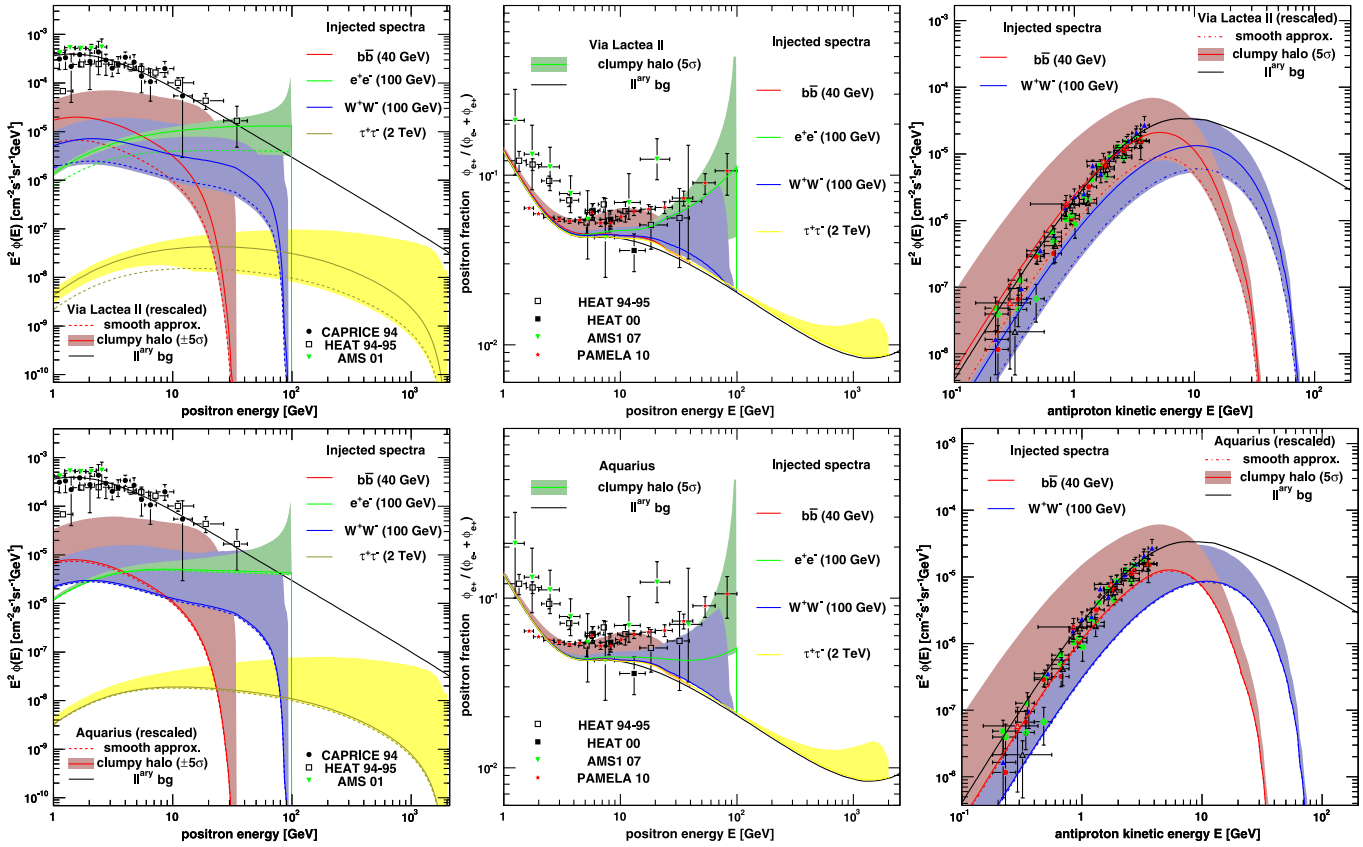

FIG. 13 (color online). Same as Fig. 11, but after having rescaled the *Via Lactea II* and *Aquarius* configurations to the same local dark matter density $\rho_\odot = 0.385$ GeV cm^{-3}.

resulting uncertainty in terms of primary positron flux can easily reach 1 order of magnitude [87,89].

3. Comments on the positron fraction

The excess in the positron fraction above a few GeV, recently made clearer with the release of PAMELA data [1], but previously hinted by the HEAT [95] and AMS data [97], has triggered an impressive number of studies, most of them dedicated to a possible DM interpretation (e.g., [73]). Most of the predictions rely on the assumption that the DM annihilation rate is boosted, essentially from the nonrelativistic Sommerfeld effect, with large branching ratios to leptons. Some others invoke, instead, DM decay with a tuned lifetime. All of these assumptions are somewhat fine-tuned, and most of them do not treat the background consistently with the primary component. Here, we provide self-consistent predictions for some benchmarks mostly motivated by particle physics (except for one leptophilic model) and, more importantly, do not demand a good fit to the PAMELA data. Instead, we aim at testing the potential imprints and the detectability of such scenarios in the antimatter spectrum.

In the central panels of Fig. 11 (see also Figs. 12 and 13), we have plotted the results for the positron flux in terms of the corresponding positron fraction, i.e., $\phi_{e^+}/(\phi_{e^+} + \phi_{e^-})$. The actual denominator of the positron fraction can be obtained by fitting the Fermi data on the sum of cosmic electrons plus positrons above 20 GeV [5], avoiding, thereby, invoking any model of primary or/and secondary component. At lower energy, we have constrained the electron spectrum from a fit on the AMS data [94], and, for positrons, we have taken the sum of our primaries plus secondaries, assuming that there are no other sources of positrons. This assumption is conservative in the sense that below 10 GeV, the secondaries dominate over all our primaries. We have linked the two domains by interpolating over a range of a few GeV.

As already discussed in Sec. V C 2, only the WIMP model annihilating in e^+e^-, with $m_\chi = 100$ GeV, provides a sizable contribution to the positron fraction, significantly overtopping the secondary prediction above 10 GeV. The other benchmark models contribute most at the percent level, except when considering 5σ subhalo fluctuations and neglecting tidal disruption. Still, our 100 GeV leptophilic model could fit the PAMELA data without any artificial boost factor, just by considering theoretically constrained dark matter distributions. This is a very appealing result. Nevertheless, we remind the reader that viable astrophysical explanations exist, like the contribution of local pulsars [12,80], and it might be difficult to distinguish between those different solutions to the positron

excess, given the limited sensitivities and energy resolutions of the current experiments (even a χ^2 analysis is hardly relevant due to the large theoretical uncertainties). Our leptophilic model would give a sharp cutoff in the positron fraction as well as in the positron flux above 100 GeV, which would nevertheless be smeared by energy resolution effects. Positron data at higher energy would really help to clarify this issue of the possible contribution of DM annihilation to the positron spectrum. Indeed, if the excess is still prominent above, say, 200 GeV, a leptophilic model could hardly fuel the dominant contribution with conventional parameters, due to the m_χ^{-4} scaling of the primary flux, when $E \to m_\chi$, compared to the $E^{-3.5}$ scaling of the secondary background [see Eq. (27)].

VI. INVERSE COMPTON SCATTERING OF ELECTRONS AND POSITRONS FROM DM ANNIHILATION ON GALACTIC PHOTONS

We finally consider the inverse Compton scattering process, which happens when the high-energy electrons and positrons produced in the DM annihilation scatter on the low-energy photons of our Galaxy. The resulting energies of the upscattered photons will be increased by a factor $\propto \gamma^2$, where γ is the Lorentz factor $\gamma = \frac{E_e}{m_e}$.

Galactic target photons include starlight photons in the optical wavelength from the stars of the Galactic disk (hereafter, SL), infrared radiation produced by the interaction of such starlight photons with the Galactic dust (IR), and the homogeneous bath of cosmic microwave background photons (CMB).

Now consider that SL/IR/CMB photons have typical mean energy of $0.3/3.5 \times 10^{-3}/2.5 \times 10^{-4}$ eV, respectively. The maximum Lorentz factor for electrons and positrons produced by the annihilation of our benchmark candidates (gotten when $E_e = m_\chi$) is of the order of $\gamma \sim 8 \times 10^4$, 2×10^5, and 4×10^6 for benchmarks A ($m_\chi = 40$ GeV), B and C ($m_\chi = 100$ GeV), and D ($m_\chi = 2$ TeV), respectively. Thus, the photons can be scattered up to energies of $10^{-3}/9 \times 10^{-3}/3.6$ GeV (CMB), $2 \times 10^{-2}/10^{-1}/53$ GeV (IR), and $2/12/462$ GeV (SL) for benchmarks A, B and C, and D, respectively. These are rough estimates of the relevant energy ranges to discuss, although we have to keep in mind that blackbody distributions spread beyond their mean values. Since we are interested in the γ-ray flux at the GeV scale, this implies that benchmark A will not give any contribution at all. As far as benchmark B is concerned, we expect its ICS contribution to γ rays to be negligible at the energies of interest, since the bulk of electrons and positrons will have energies much lower than m_χ (we recall that the annihilation channel is W^+W^-).

We will, then, restrict ourselves to the computation of ICS processes for benchmarks C and D, which on the other hand do not produce any significant γ-ray flux from the prompt emission.

A. The inverse Compton scattering computation

The ICS γ-ray spectrum is given by

$$\frac{d\Phi}{d\epsilon_1} = \frac{1}{\epsilon_1} \int_{\Delta\Omega} d\Omega \int_{\rm los} ds \frac{j(\epsilon_1, r)}{4\pi}. \tag{28}$$

Here, ϵ is the energy of the original photon, and ϵ_1 the energy of the scattered photon. $j(\epsilon_1, r)$ is the emissivity given by

$$j(\epsilon_1, r) = 2 \int_{m_e}^{M_{\rm DM}} dE \mathcal{P}(\epsilon_1, E, r) n_e(r, E), \tag{29}$$

which carries units of inverse volume and inverse time. Here, $\mathcal{P}(\epsilon_1, E, r)$ is the differential power emitted into photons of energy ϵ_1 by an electron with energy E. We refer to [102,103] for its explicit form. We just recall that the emitted power is given by the rate of scattering $dN_{E,\epsilon}/dtd\epsilon_1$ of high-energy electrons on photons of energy ϵ into photons of energy ϵ_1, times the energy lost in a scattering $(\epsilon_1 - \epsilon)$, integrated over all initial photon energies. The rate of scattering is proportional to the energy density of the photon bath $n(\epsilon, r)$. Finally, $n_e(r, E)$ is the electron number density.

At variance with [103], we compute $n_e(r, E)$ by solving the diffusion-loss equation in the Galactic disk, as explained in Sec. VA. Indeed, we have computed the electron-positron flux at 3 different distances from the GC, both in the diffusionless and in the complete case. We find that the difference between the two cases gets larger when getting closer to the GC, as expected, and as illustrated in the left panel of Fig. 14. This confirms that the diffusionless approximation is not valid at all in the steady state regime when the injection rate varies significantly over a typical diffusion length, like, for example, in the Galactic center.

Following [103], we model the total radiation density as a superposition of three blackbodylike spectra of the form

$$n_a(\epsilon, r) = \mathcal{N}_a(r) \frac{\epsilon^2}{\pi^2} \frac{1}{(e^{\epsilon/T} - 1)}, \tag{30}$$

with different temperatures $T_{\rm CMB} = 2.5 \times 10^{-4}$ eV, $T_{\rm IR} = 3.5 \times 10^{-3}$ eV, and $T_{\rm SL} = 0.3$ eV. Yet, here, we are not interested in averaging our signal on large parts of the sky, while we want to study the angular dependence of the ICS flux for solid angles $\Delta\Omega = 10^{-5}$ sr to be comparable with the prompt γ-ray flux and to be predictive for Fermi all-sky observations. Hence, we cannot set $\mathcal{N}_a$ as a constant as in [103].

We fit the results of [104,105] to model the ρ and z dependence of $\mathcal{N}_a$, where ρ and z are cylindrical coordinates along and perpendicular to the Galactic plane. We find that $\mathcal{N}_a(\rho, z)$ can be written as a function of a constant $\mathcal{N}_a^{\rm GC}$ computed at $\rho = z = 0$. Values of $\mathcal{N}_a^{\rm GC}$

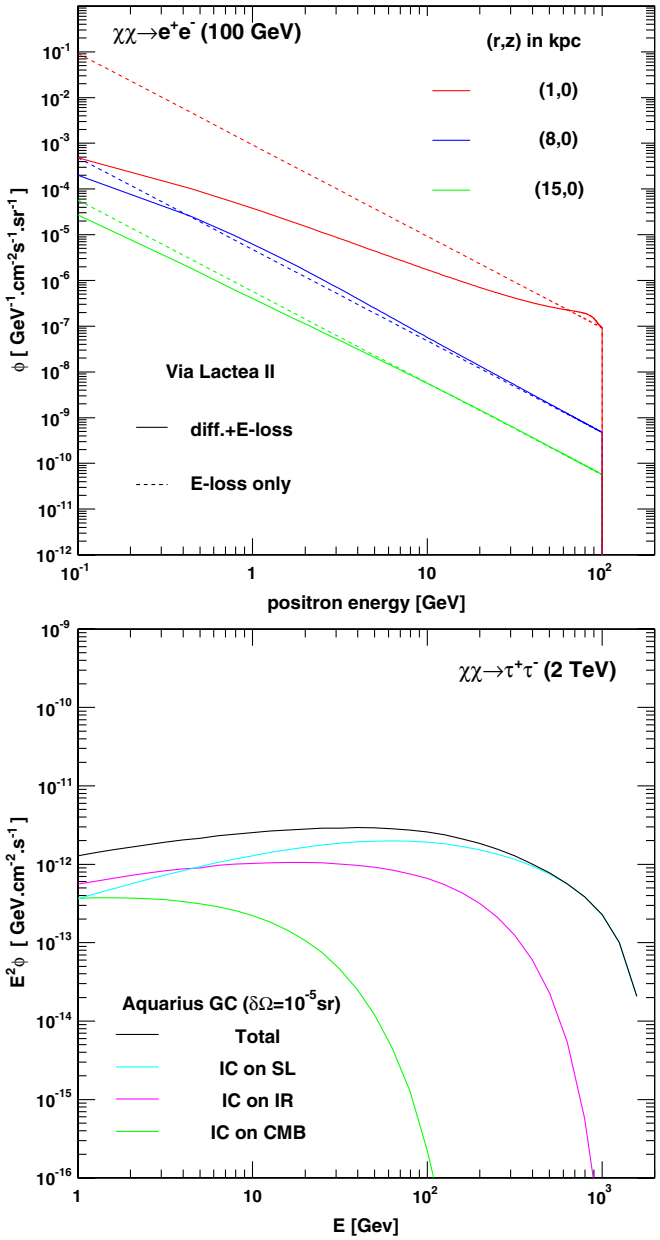

FIG. 14 (color online). Top: Template comparison between the positron fluxes predicted at different radii in the *Via Lactea II* setup (in the smooth approximation) in a full propagation model (solid curves) and in a model considering the energy losses only. Bottom: Predictions of the IC flux generated by benchmark D in the direction of the GC for both the *Aquarius* and *Via Lactea II* configurations.

can be found in [103]: $\mathcal{N}^{\rm GC}_{\rm CMB} = 1$, $\mathcal{N}^{\rm GC}_{\rm IR} = 7 \times 10^{-5}$, and $\mathcal{N}^{\rm GC}_{\rm SL} = 1.7 \times 10^{-11}$. For the CMB, obviously, $\mathcal{N}_{\rm CMB}(\rho, z) = \mathcal{N}^{\rm GC}_{\rm CMB} = 1$.

In the SL case, we obtain the following fits:

$$\mathcal{N}_{\rm SL}(\rho, z) = \begin{cases} \mathcal{N}^{\rm GC}_{\rm SL} e^{-\alpha_{\rm SL}\rho} & z \le 0.2 \text{ kpc} \\ A_{\rm SL} \times \mathcal{N}^{\rm GC}_{\rm SL} e^{-\alpha_{\rm SL}\rho} e^{-\beta_{\rm SL} z} & z > 0.2 \text{ kpc} \end{cases}. \tag{31}$$

For the IR case, we get

$$\mathcal{N}_{\rm IR}(\rho, z) = \begin{cases} (\mathcal{N}^{\rm GC}_{\rm IR} - B_{\rm IR}\rho) e^{-\beta_{\rm IR} z} & \rho \le 4 \text{ kpc} \\ A_{\rm IR} \times \mathcal{N}^{\rm GC}_{\rm IR} e^{-\alpha_{\rm IR}\rho} e^{-\beta_{\rm IR} z} & \rho > 4 \text{ kpc} \end{cases}, \tag{32}$$

with $\alpha_{\rm SL} \sim 0.47$, $\beta_{\rm SL} \sim 0.57$, $A_{\rm SL} \sim 1.12$, $\alpha_{\rm IR} \sim 0.33$, $\beta_{\rm IR} \sim 0.43$, $A_{\rm IR} \sim 2.29$, and $B_{\rm IR} \sim 6.6 \times 10^{-6}$.

B. Results

We have computed the γ-ray flux from ICS for our particle physics benchmarks C and D. The results are shown in Figs. 14 and 15. The bottom panel of Fig. 14

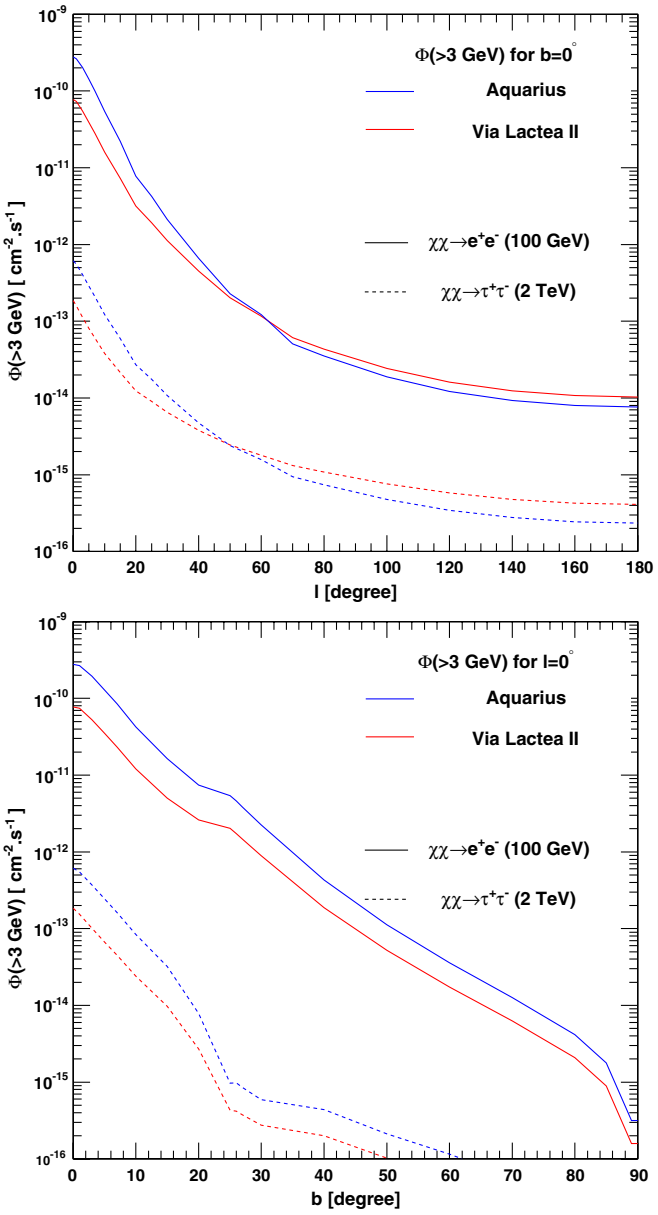

FIG. 15 (color online). Top: Longitudinal dependence of the IC integrated flux ($b = 0°$) obtained for *Aquarius* and *Via Lactea II*. Bottom: Latitude dependence ($l = 0°$).

displays the flux predicted in the direction of the GC (for benchmark D only), while Fig. 15 shows the longitude (top) and latitude (bottom) dependence on the integrated flux at null latitude and longitude, respectively.

We note that the ICS γ-ray flux produced by electrons and positrons deriving from the annihilation of particles described by our benchmarks C and D are not in conflict with the available data on γ rays. In fact, [103] have shown that benchmark C (D) would need a cross section 1 (3) order(s) of magnitude larger than the thermal one in order to overproduce photons with respect to the EGRET and Fermi diffuse backgrounds. We note also that the predictions performed in the *Aquarius* configuration overtop the ones calculated in the *Via Lactea II* configuration towards the central regions of the Galaxy, where the dark matter annihilation rate is set by the smooth halo, whereas the hierarchy reverses at larger longitudes where subhalos come into play. This is due to the larger mass fraction and the relative domination of the lightest subhalos occurring in the *Via Lactea II* setup.

We have also checked our predictions against the preliminary Fermi observation of the 1° region around the Galactic center [106]. We find that benchmark D is a few orders of magnitude below such a signal. In the case of benchmark C, the predicted flux does not exceed the observed one, although it reaches one-third of its value at energies around 20 GeV. We, therefore, conclude that the ICS contribution to the γ-ray flux is likely not observable for the leptophilic benchmarks that we selected in this paper.

VII. CONCLUSIONS

We have studied the γ-ray and antimatter fluxes arising in two astrophysical setups built on the *Aquarius* and *Via Lactea II* high-resolution N-body simulations. Our aim was to quantify the differences between the two simulations in terms of prospects for detection and to assess the impact of extrapolating the mass function and concentration of subhalos down to their minimum mass, which for common DM candidates can be 10 orders of magnitude smaller than the mass resolution of simulations. We stress that the two simulations are in remarkable agreement with each other, and that the biggest differences in the prospects for detection arise from the different extrapolations of physical quantities suggested by different groups of authors (as in the case of the mass function of subhalos) and from the application of the results of the simulations to the specific MW halo. We present our results for the *Aquarius* and *Via Lactea II* setups, meaning that they correspond to models that we have built on simulations and not to the simulations, themselves.

We have studied the different contributions to the γ-ray flux arising from the smooth DM halo of the MW, resolved subhalos (that we have generated with a Monte Carlo procedure), unresolved subhalos, and extragalactic halos and subhalos. The smooth component dominates the annihilation flux in the inner regions of the Galaxy. In the *Via Lactea II* setup, the resolved and unresolved subhalos dominate the annihilation flux at angles larger than ~ 20 degrees from the GC, all the way to the anticenter, where the extragalactic flux becomes comparable, although never dominant. In the *Aquarius* setup, the substructure component is suppressed and never exceeds the smooth component. The extragalactic flux becomes, instead, dominant at angles larger than $\sim$60 degrees from the GC.

We have provided full-sky maps that can be used as templates for DM searches with current experiments such as Fermi. If the search is concentrated towards the GC, there is little difference between the two simulations, in the sense that the profile of the annihilation flux is very similar in the two setups, while the normalization must be kept free, given the uncertainties of the particle physics parameters. The optimal strategy to search for an annihilation signal is to take the sky maps provided by Fermi, which will constitute the ''background,'' and take our DM templates as signal. One can, then, easily estimate the size and shape of the region around the GC that maximizes the S/N ratio.

For a fixed particle physics model, the annihilation flux from the central regions of the Galaxy in the *Via Lactea II* setup is slightly smaller with respect to *Aquarius*. This is due to the smaller local density, i.e., DM density in the solar neighborhood, in the *Via Lactea II* setup and the smaller total mass. If one rescales the *Via Lactea II* and *Aquarius* setups to match the most recent determinations of the local density, and if the same subhalo mass fraction $f_{\rm cl} = 0.18$ is adopted for both simulations, then the annihilation maps look almost identical.

Should the search for the diffuse emissions from the GC fail because of the complicated astrophysical backgrounds in what is probably the most crowded region of the sky, the possibility remains to search for unidentified γ-ray sources, which would appear as nonvariable bright spots with no astrophysical counterpart, possibly correlated with dwarf galaxies, and with identical spectra. The number of detectable sources in both simulation setups is very similar, and for an optimistic DM scenario is between 1 and 10 for the Fermi-LAT in 5 years of operation.

Finally, we have calculated the antimatter fluxes in both simulation setups, and we found that the boost factors often invoked to provide a viable DM interpretation of the cosmic leptons puzzle are completely unrealistic, if attributed to a subhalo population. The only annihilation channel that provides a sizeable enhancement of the positron ratio is direct annihilation to e^+e^- around 100 GeV, which provides a flux significantly higher than the secondary background for the set of propagation parameters used here, even without the help of any subhalo contribution. We have also verified that the associated ICS contribution to the γ-ray flux was not violating the current observational

constraints. Although this model seems an appealing possibility, we still stress that (i) it has been tuned to provide an exception case to the usual need for a large boost factor to interpret the PAMELA data [see Eq. (27) and comments below] without any particle physics motivation, (ii) slightly increasing the DM particle mass above 100 GeV would completely erase such a peak with respect to the background because of the dependency of the peak amplitude in m_χ^{-4} and the steep decrease of the flux at lower energies, and (iii) we did not include the contributions of other astrophysical primary sources, like pulsars, which are likely sizable.

ACKNOWLEDGMENTS

We would like to thank J. Diemand and M. Fornasa for useful discussions. E. B. thanks the Institut d'Astrophysique de Paris for the kind hospitality. L. P. also thanks the Department of Physics of the University of Trento for the kind hospitality. E. B. and L. P. acknowledge financial contribution from Contract No. ASI-INAF/TH-018. This work was supported in part by the French ANR project ToolsDMColl, BLAN07-2-194882.

APPENDIX: SMOOTH VERSUS SUBHALO MASS-DENSITY PROFILES FOR ANTIBIASED RELATIONS

The spatial distribution of subhalos has long been modeled with a cored isothermal profile, e.g., as suggested in Ref. [107]. Nevertheless, it turns out that such a spatial distribution is hardly consistent with a global NFW fit on the overall DM distribution, which scales like r^{-3} at large radii, at variance with the r^{-2} isothermal behavior. Indeed, subhalos are usually found to dominate the mass profile at radii larger than the scale radius (~ 20 kpc), so one could expect their mass-density profile to track the r^{-3} shape of the overall fit. In Ref. [108], the authors quoted the same previous reference and proposed the following empirical spatial distribution for the subhalo number density $n(r)$, the so-called *antibiased* distribution:

$$n(r) \propto r\rho_{\rm host}(r). \tag{A1}$$

Considering that $\rho_{\rm host}$ is the overall fit, this would lead to the same issue as above: for a global NFW profile, the subhalo distribution would decrease like r^{-2} beyond the scale radius, which is inconsistent with the fact that they are found to dominate the mass profile on large radii. For consistency, $\rho_{\rm host}$ should, thereby, be the *smooth* DM component instead.

In this appendix, we sketch an analytical method to model any antibiased subhalo distribution, given a defined overall density profile.

1. General case

Let us consider that a global fit on an N-body galaxy made of pure dark matter provides an analytical shape for the overall mass-density profile, $\rho_{\rm tot}(r)$. This density profile must, therefore, obey

$$4\pi \int_0^{R_{\rm vir}} dr r^2 \rho_{\rm tot}(r) = M_{\rm MW}. \tag{A2}$$

In the following, we will consider that $M_{\rm MW}$, $R_{\rm vir}$, and $\rho_{\rm tot}$ are known.

Now, let us assume that this overall profile is, in fact, made of two subcomponents, one describing the smooth distribution of dark matter, $\rho_{\rm sm}(r)$, and another accounting for the mass density carried by subhalos, $\rho_{\rm sub}(r)$. If we know the mass fraction of resolved subhalos in any N-body galaxy, and if we further know the mass distribution of these objects, then assuming a scale-invariant mass profile allows us to determine the total mass fraction $f_{\rm sub}^{\rm tot}$ for any arbitrary minimal mass for subhalos. Therefore, the total mass-density profile may be rewritten as

$$\begin{aligned}\rho_{\rm tot}(r) &= \rho_{\rm sm}(r) + \rho_{\rm sub}(r) \\ &= (1 - f_{\rm sub}^{\rm tot}) M_{\rm MW} g_{\rm sm}(r) + f_{\rm sub}^{\rm tot} M_{\rm MW} g_{\rm sub}(r),\end{aligned} \tag{A3}$$

where $g_{\rm sm}(r)$ and $g_{\rm sub}(r)$ are normalized to unity inside a spherical volume delineated by $R_{\rm vir}$. We have merely used the fact that the total mass in the form of subhalos is $M_{\rm sub}^{\rm tot} = f_{\rm sub}^{\rm tot} M_{\rm MW}$.

If we further assume that the subhalo spatial distribution $g_{\rm sub}(r)$ is antibiased with respect to the smooth distribution $g_{\rm sm}(r)$, then we have the following relation:

$$g_{\rm sub}(r) = K r g_{\rm sm}(r), \tag{A4}$$

where K is a constant that ensures the normalization to unity inside a sphere of radius $R_{\rm vir}$.

From this, we can readily express $g_{\rm sm}(r)$ or $g_{\rm sub}(r)$ in terms of the known quantities. For the former one, we find:

$$g_{\rm sm}(r) = \frac{\rho_{\rm tot}(r)}{(1 - f_{\rm sub}^{\rm tot}) M_{\rm MW}\left[1 + \frac{r}{r_b}\right]}, \tag{A5}$$

where we have defined the *bias radius* r_b as follows:

$$r_b \equiv \frac{(1 - f_{\rm sub}^{\rm tot})}{f_{\rm sub}^{\rm tot} K}. \tag{A6}$$

All parameters are known, except the constant K. However, it can easily be derived from this equation by demanding that $g_{\rm sm}(r)$ is normalized to unity inside a sphere of radius $R_{\rm vir}$. We can further verify that this value obtained for K automatically ensures the normalization of $g_{\rm sub}(r)$ as expressed in Eq. (A4).

TABLE V. Parameters relevant for the *Via Lactea II* setup. The Sun position is taken at 8 kpc.

$R_{\rm MW}$ (kpc)	$M_{\rm MW}$ ($M_\odot$)	r_s (kpc)	r_b (kpc)	ρ_s (GeV/cm^3)	slope α	$M_{\rm sub}^{\rm tot}$ ($M_\odot$)	$f_{\rm sub}^{\rm tot}$ (%)	$\rho_\odot$ (GeV/cm^3)	$\rho_{\odot,\rm sm}$ (GeV/cm^3)	$\rho_{\odot,\rm sub}$ (GeV/cm^3)
402	1.9×10^{12}	21	85.5	0.31	2.0	10^{12}	53.3	0.42	0.39	0.03

It is interesting to derive the expression for the smooth density profile

$$\rho_{\rm sm}(r) = (1 - f_{\rm sub}^{\rm tot}) M_{\rm MW} g_{\rm sm}(r) = \frac{\rho_{\rm tot}(r)}{(1 + r/r_b)}. \quad \text{(A7)}$$

Similarly, we can determine the averaged subhalo mass-density profile:

$$\rho_{\rm sub}(r) = f_{\rm sub}^{\rm tot} M_{\rm MW} K r g_{\rm sm}(r) = \frac{\rho_{\rm tot}(r)(r/r_b)}{(1 + r/r_b)}. \quad \text{(A8)}$$

One can readily check that $\rho_{\rm sm}(r) + \rho_{\rm sub}(r) = \rho_{\rm tot}(r)$, as required.

We can now interpret the physical meaning of the bias radius. This radius actually provides the scale beyond which the smooth profile departs from the total density profile, more precisely beyond which the smooth density decreases one power of r faster than the overall density, since the mass density in subhalos starts to dominate. In *Via Lactea II*, where the overall density is well-fitted with an NFW profile, the bias radius is of the order of the NFW scale radius. Thus, the smooth profile is found to scale like r^{-1} in the central regions of the Galaxy, while it falls like r^{-4} in the outer skirts, faster than the r^{-3} behavior of the NFW shape.

2. Application to *Via Lactea II*

As a useful application, we will use the *Via Lactea II* setup, for which the parameters are recalled in Table V. We remind that the NFW profile is given by

$$\rho_{\rm tot}(r) = \frac{\rho_s (r_s/r)}{(1 + r/r_s)^2}. \quad \text{(A9)}$$

If we assume a mass profile for subhalos of the form $\propto m^{-\alpha}$ and impose that a certain fraction $f_{\rm ref}$ of the Milky Way mass is carried by subhalos in the mass range $[m_{\rm ref}, m_{\rm max}]$, then the total mass fraction in subhalos $f_{\rm sub}^{\rm tot}$ is entirely fixed by the minimal subhalo mass $m_{\rm min}$.

In the antibiased hypothesis, the smooth density profile is defined by Eqs. (A5) and (A7). In particular, we have defined the function $g_{\rm sm}$ such that it is normalized to unity over the Galaxy volume. It turns out that this volume integral has an analytical form in the *Via Lactea II* setup:

$$1 = 4\pi \int_0^{R_{\rm vir}} dr r^2 g_{\rm sm}(r) = 4\pi r_b r_s^3 \rho_s \frac{\left[R_{\rm vir}(r_s - r_b) + r_b (R_{\rm vir} + r_s) \ln\left\{ \frac{r_b (R_{\rm vir} + r_s)}{r_s (r_b + R_{\rm vir})} \right\} \right]}{(1 - f_{\rm sub}^{\rm tot}) M_{\rm MW} (r_b - r_s)^2 (R_{\rm vir} + r_s)}, \quad \text{(A10)}$$

such that we can easily compute the value of r_b that ensures the normalization to unity. The full results are summarized in Table V.

[1] O. Adriani, G. C. Barbarino, and G. A. Bazilevskaya *et al.*, Nature (London) **458**, 607 (2009).
[2] J. Chang, J. H. Adams, and H. S. Ahn *et al.*, Nature (London) **456**, 362 (2008).
[3] F. Aharonian, A. G. Akhperjanian, and U. Barres de Almeida *et al.*, Phys. Rev. Lett. **101**, 261104 (2008).
[4] F. Aharonian, A. G. Akhperjanian, and G. Anton *et al.*, Astron. Astrophys. **508**, 561 (2009).
[5] A. A. Abdo, M. Ackermann, and M. Ajello *et al.*, Phys. Rev. Lett. **102**, 181101 (2009).
[6] D. Hooper, P. Blasi, and P. Dario Serpico, J. Cosmol. Astropart. Phys. 01 (2009) 025.
[7] S. Profumo, arXiv:0812.4457.
[8] D. Grasso (Fermi-LAT Collaboration), arXiv:0907.0373.
[9] P. Blasi, Phys. Rev. Lett. **103**, 051104 (2009).
[10] T. Piran, N. J. Shaviv, and E. Nakar, arXiv:0905.0904.
[11] H. Yuksel, M. D. Kistler, and T. Stanev, Phys. Rev. Lett. **103**, 051101 (2009).
[12] T. Delahaye, J. Lavalle, R. Lineros, F. Donato, and N. Fornengo, Astron. Astrophys. **524**, A51 (2010).
[13] M. Cirelli, M. Kadastik, M. Raidal, and A. Strumia, Nucl. Phys. **B813**, 1 (2009).
[14] N. Arkani-Hamed, D. P. Finkbeiner, T. R. Slatyer, and N. Weiner, Phys. Rev. D **79**, 015014 (2009).
[15] G. Bertone, M. Cirelli, A. Strumia, and M. Taoso, J. Cosmol. Astropart. Phys. 03 (2009) 009.
[16] L. Bergstrom, G. Bertone, T. Bringmann, J. Edsjö, and M. Taoso, Phys. Rev. D **79**, 081303 (2009).
[17] M. Pato, L. Pieri, and G. Bertone, Phys. Rev. D **80**, 103510 (2009).
[18] E. Borriello, A. Cuoco, and G. Miele, Astrophys. J. Lett. **699**, L59 (2009).

[19] A. V. Belikov and D. Hooper, Phys. Rev. D **81**, 043505 (2010).
[20] S. Profumo and T. E. Jeltema, J. Cosmol. Astropart. Phys. 07 (2009) 020.
[21] R. Catena, N. Fornengo, M. Pato, L. Pieri, and A. Masiero, Phys. Rev. D **81**, 123522 (2010).
[22] S. Galli, F. Iocco, G. Bertone, and A. Melchiorri, Phys. Rev. D **80**, 023505 (2009).
[23] T. R. Slatyer, N. Padmanabhan, and D. P. Finkbeiner, Phys. Rev. D **80**, 043526 (2009).
[24] M. Cirelli, F. Iocco, and P. Panci, J. Cosmol. Astropart. Phys. 10 (2009) 009.
[25] L. Bergstrom, P. Ullio, and J. H. Buckley, Astropart. Phys. **9**, 137 (1998).
[26] L. Bergstrom, T. Bringmann, M. Eriksson, and M. Gustafsson, J. Cosmol. Astropart. Phys. 04 (2005) 004.
[27] T. Bringmann, L. Bergstrom, and J. Edsjo, J. High Energy Phys. 01 (2008) 049.
[28] J. F. Beacom, N. F. Bell, and G. Bertone, Phys. Rev. Lett. **94**, 171301 (2005).
[29] G. Bertone, C. B. Jackson, G. Shaughnessy, T. M. P. Tait, and A. Vallinotto, Phys. Rev. D **80**, 023512 (2009).
[30] E. A. Baltz, C. Briot, P. Salati, R. Taillet, and J. Silk, Phys. Rev. D **61**, 023514 (1999).
[31] L. Pieri and E. Branchini, Phys. Rev. D **69**, 043512 (2004).
[32] N. W. Evans, F. Ferrer, and S. Sarkar, Phys. Rev. D **69**, 123501 (2004).
[33] S. M. Koushiappas, A. R. Zentner, and T. P. Walker, Phys. Rev. D **69**, 043501 (2004).
[34] A. Tasitsiomi, in *High Energy Gamma-Ray Astronomy*, edited by F. A. Aharonian, H. J. Volk, and D. Horns, AIP Conf. Proc. No. 745 (AIP, New York, 2005).
[35] L. Bergstrom and D. Hooper, Phys. Rev. D **73**, 063510 (2006).
[36] G. Bertone, A. R. Zentner, and J. Silk, Phys. Rev. D **72**, 103517 (2005).
[37] S. Horiuchi and S. Ando, Phys. Rev. D **74**, 103504 (2006).
[38] S. Colafrancesco, S. Profumo, and P. Ullio, Phys. Rev. D **75**, 023513 (2007).
[39] M. Fornasa and G. Bertone, Int. J. Mod. Phys. D **17**, 1125 (2008).
[40] L. Pieri, G. Bertone, and E. Branchini, Mon. Not. R. Astron. Soc. **384**, 1627 (2008).
[41] L. Pieri, A. Pizzella, E. M. Corsini, E. Dalla Bontã, and F. Bertola, Astron. Astrophys. **496**, 351 (2009).
[42] S. Ando, M. Kamionkowski, S. K. Lee, and S. M. Koushiappas, Phys. Rev. D **78**, 101301 (2008).
[43] S. Ando and E. Komatsu, Phys. Rev. D **73**, 023521 (2006).
[44] S. Ando, E. Komatsu, T. Narumoto, and T. Totani, Phys. Rev. D **75**, 063519 (2007).
[45] A. Cuoco, J. Brandbyge, S. Hannestad, T. Haugbølle, and G. Miele, Phys. Rev. D **77**, 123518 (2008).
[46] A. Cuoco, S. Hannestad, T. Haugbølle, G. Miele, P. D. Serpico, and H. Tu, J. Cosmol. Astropart. Phys. 04 (2007) 013.
[47] J. M. Siegal-Gaskins, J. Cosmol. Astropart. Phys. 10 (2008) 040.
[48] J. M. Siegal-Gaskins and V. Pavlidou, Phys. Rev. Lett. **102**, 241301 (2009).
[49] S. Ando, Phys. Rev. D **80**, 023520 (2009).
[50] S. Dodelson, A. V. Belikov, D. Hooper, and P. Serpico, Phys. Rev. D **80**, 083504 (2009).
[51] M. Fornasa, L. Pieri, G. Bertone, and E. Branchini, Phys. Rev. D **80**, 023518 (2009).
[52] C. Lacey and S. Cole, Mon. Not. R. Astron. Soc. **262**, 627 (1993).
[53] R. E. Angulo and S. D. M. White, arXiv:0906.1730.
[54] J. Diemand, M. Kuhlen, and P. Madau, Astrophys. J. **657**, 262 (2007).
[55] J. Diemand, M. Kuhlen, P. Madau, M. Zemp, B. Moore, D. Potter, and J. Stadel, Nature (London) **454**, 735 (2008).
[56] V. Springel, S. D. M. White, and C. S. Frenk *et al.*, Nature (London) **456**, 73 (2008).
[57] V. Springel, J. Wang, and M. Vogelsberger *et al.*, Mon. Not. R. Astron. Soc. **391**, 1685 (2008).
[58] J. Diemand, B. Moore, and J. Stadel, Nature (London) **433**, 389 (2005).
[59] J. Lavalle, J. Pochon, P. Salati, and R. Taillet, Astron. Astrophys. **462**, 827 (2007).
[60] A. A. Abdo, M. Ackermann, and M. Ajello *et al.*, Phys. Rev. Lett. **103**, 251101 (2009).
[61] G. Dobler, D. P. Finkbeiner, I. Cholis, T. R. Slatyer, and N. Weiner, Astrophys. J. **717**, 825 (2010).
[62] A. N. Cillis and R. C. Hartman, Astrophys. J. **621**, 291 (2005).
[63] F. Donato, D. Maurin, P. Salati, A. Barrau, G. Boudoul, and R. Taillet, Astrophys. J. **563**, 172 (2001).
[64] T. Delahaye, F. Donato, N. Fornengo, J. Lavalle, R. Lineros, P. Salati, and R. Taillet, Astron. Astrophys. **501**, 821 (2009).
[65] J. Dunkley, E. Komatsu, and M. R. Nolta *et al.*, Astrophys. J. Suppl. Ser. **180**, 306 (2009).
[66] M. Kuhlen, J. Diemand, and P. Madau, Astrophys. J. **686**, 262 (2008).
[67] M. Kuhlen, J. Diemand, and P. Madau, Astrophys. J. **671**, 1135 (2007).
[68] Y.-S. Li and S. D. M. White, Mon. Not. R. Astron. Soc. **384**, 1459 (2008).
[69] F. D. Kahn and L. Woltjer, Astrophys. J. **130**, 705 (1959).
[70] V. Berezinsky, V. Dokuchaev, and Y. Eroshenko, Phys. Rev. D **77**, 083519 (2008).
[71] E. Hayashi, J. F. Navarro, J. E. Taylor, J. Stadel, and T. Quinn, Astrophys. J. **584**, 541 (2003).
[72] J. Lavalle, Q. Yuan, D. Maurin, and X.-J. Bi, Astron. Astrophys. **479**, 427 (2008).
[73] L. Bergstrom, T. Bringmann, and J. Edsjo, Phys. Rev. D **78**, 103520 (2008).
[74] N. Fornengo, L. Pieri, and S. Scopel, Phys. Rev. D **70**, 103529 (2004).
[75] J. S. Bullock, T. S. Kolatt, and Y. Sigad *et al.*, Mon. Not. R. Astron. Soc. **321**, 559 (2001).
[76] P. Ullio, L. Bergstrom, J. Edsjo, and C. Lacey, Phys. Rev. D **66**, 123502 (2002).
[77] R. Catena and P. Ullio, J. Cosmol. Astropart. Phys. 08 (2010) 004.
[78] L. E. Strigari and R. Trotta, J. Cosmol. Astropart. Phys. 11 (2009) 019.
[79] J. Silk and M. Srednicki, Phys. Rev. Lett. **53**, 624 (1984).
[80] A. Boulares, Astrophys. J. **342**, 807 (1989).

[81] M. S. Longair, *Stars, the Galaxy, and the Interstellar Medium*, High Energy Astrophysics Vol. 2 (Cambridge University Press, Cambridge, England 1994), 2nd ed..
[82] D. Maurin, F. Donato, R. Taillet, and P. Salati, Astrophys. J. **555**, 585 (2001).
[83] V. S. Berezinskii, S. V. Bulanov, V. A. Dogiel, and V. S. Ptuskin, in *Astrophysics of Cosmic Rays*, edited by V. L. Ginzburg (North-Holland, Amsterdam, 1990).
[84] V. L. Ginzburg and S. I. Syrovatskii, *The Origin of Cosmic Rays* (Macmillan, New York, 1964).
[85] A. W. Strong, I. V. Moskalenko, and V. S. Ptuskin, Annu. Rev. Nucl. Part. Sci. **57**, 285 (2007).
[86] D. Maurin, R. Taillet, F. Donato, P. Salati, A. Barrau, and G. Boudoul, arXiv:astro-ph/0212111.
[87] F. Donato, N. Fornengo, D. Maurin, P. Salati, and R. Taillet, Phys. Rev. D **69**, 063501 (2004).
[88] E. A. Baltz and J. Edsjo, Phys. Rev. D **59**, 023511 (1998).
[89] T. Delahaye, R. Lineros, F. Donato, N. Fornengo, and P. Salati, Phys. Rev. D **77**, 063527 (2008).
[90] J. Lavalle, E. Nezri, E. Athanassoula, F.-S. Ling, and R. Teyssier, Phys. Rev. D **78**, 103526 (2008).
[91] J. Silk and A. Stebbins, Astrophys. J. **411**, 439 (1993).
[92] M. Boezio, P. Carlson, and T. Francke *et al.*, Astrophys. J. **532**, 653 (2000).
[93] M. A. DuVernois, S. W. Barwick, and J. J. Beatty *et al.*, Astrophys. J. **559**, 296 (2001).
[94] M. Aguilar, J. Alcaraz, and J. Allaby *et al.*, Phys. Rep. **366**, 331 (2002).
[95] S. W. Barwick, J. J. Beatty, and A. Bhattacharyya *et al.*, Astrophys. J. Lett. **482**, L191 (1997).
[96] J. J. Beatty, A. Bhattacharyya, and C. Bower *et al.*, Phys. Rev. Lett. **93**, 241102 (2004).
[97] M. Aguilar, J. Alcaraz, and J. Allaby *et al.*, Phys. Lett. B **646**, 145 (2007).
[98] S. Orito, T. Maeno, and H. Matsunaga *et al.*, Phys. Rev. Lett. **84**, 1078 (2000).
[99] T. Maeno, S. Orito, and H. Matsunaga *et al.*, Astropart. Phys. **16**, 121 (2001).
[100] Y. Asaoka, Y. Shikaze, and K. Abe *et al.*, Phys. Rev. Lett. **88**, 051101 (2002).
[101] S. Haino *et al.*, in *Proceedings of the 29th International Cosmic Ray Conference, Pune, India, 2005* (Tata Institute of Fundamental Research, Mumbai, 2005), Vol. 3, p. 13.
[102] G. R. Blumenthal and R. J. Gould, Rev. Mod. Phys. **42**, 237 (1970).
[103] M. Cirelli and P. Panci, Nucl. Phys. **B821**, 399 (2009).
[104] T. A. Porter *et al.*, in *Proceedings of the 29th International Cosmic Ray Conference, Pune, India, 2005* (Tata Institute of Fundamental Research, Mumbai, 2005), Vol. 4, p. 77.
[105] T. A. Porter, I. V. Moskalenko, A. W. Strong, E. Orlando, and L. Bouchet, Astrophys. J. **682**, 400 (2008).
[106] J. Cohen-Tanugi (Fermi Collaboration), in *Proceedings of the Fermi Symposium, Washington, D.C., 2009*, econf C0911022 (2009).
[107] J. Diemand, B. Moore, and J. Stadel, Mon. Not. R. Astron. Soc. **352**, 535 (2004).
[108] J. Diemand, M. Kuhlen, and P. Madau, Astrophys. J. **667**, 859 (2007).